

Detailed Experimental Measurements of Heat Transfer Augmentation in Internal Channels Using a Thermo-chromic Liquid Crystal Technique

Kartikeya Tyagi

Thesis submitted to the faculty of the
Virginia Polytechnic Institute and State University
in partial fulfillment of the requirements for the degree of

Master of Science
In
Mechanical Engineering

Srinath V. Ekkad, Chair
Wing F. Ng
Brian Vick

May 1, 2015
Blacksburg, VA

Keywords: Heat Transfer, Gas Turbine Cooling, Internal Channel Cooling,
Thermo-chromic Liquid Crystal Technique

Copyright 2015, Kartikeya Tyagi

Detailed Experimental Measurements of Heat Transfer Augmentation in Internal Channels Using a Thermochromic Liquid Crystal Technique

Kartikeya Tyagi

Abstract

Design of internal cooling channels for gas turbine blade is critical to system performance. To achieve maximum efficiency, i.e. maximum cooling with minimum coolant usage, intensive research is required to optimize heat transfer enhancement features. The present study aims at experimental and numerical investigation of two heat transfer augmentation techniques for internal cooling, viz. dimple and swirl induced jet impingement. Dimples are suitable candidates for high performance enhancement as they impose a low pressure drop penalty. The present study aims at experimentally measuring heat transfer on all the walls of diamond, triangular, square and cylindrical shaped dimples in a staggered configuration at three flow conditions in a high aspect ratio channel. A thermal-hydraulic performance factor was evaluated to characterize each dimple shape. Numerical simulations were conducted to visualize flow patterns which was correlated with heat transfer distribution. The results were in good agreement with previous studies. Triangular dimples showed the highest overall performance due to lowest pressure drop penalty, but heat transfer was low inside the dimples. In rotating channels, Coriolis Effect and centrifugal buoyancy significantly affect heat transfer distribution. There is a need to develop a cooling geometry that benefits from rotation and provides consistent cooling. A new geometry was derived from a past study, consisting of two channels divided by a wall with angled holes to provide jet impingement from inlet to outlet channel. Liquid crystal technique was used for heat transfer measurements. It was found that at high rotational speeds, heat transfer increased in the inlet channel, while it decreased in the outlet channel. Additional testing at even higher speeds may provide insight into replacing a traditional U-bend channel in a turbine blade.

Dedicated to my grandparents, Janaki and Om Prakash Tyagi

Acknowledgements

The completion of this work would not have been possible without support from several people. Foremost, I would like to thank my advisor, Dr. Srinath Ekkad, for giving me an opportunity to work under him and guiding me in every step of my work. He creates a nurturing environment for his students and promotes development of thoughts and ideas. My four years of working under Dr. Ekkad have been fantastic and a great learning experience. Next, I would like to thank the professors during my Bachelor's at Virginia Tech, Dr. Chris Williams, Dr. Wing Ng, Dr. Mark Paul and Dr. Tom Diller, for enticing me to the field of mechanical engineering and teaching me the basics that I may use in my career as a mechanical engineer. I would also like to thank Dr. Brian Vick for a great course in heat conduction and thermal system analysis.

My gratitude goes to Dr. Jaideep Pandit and Sridharan Ramesh for providing me with their assistance and advice on my projects. I would like to thank my friends, Kris Barboza, Prashant Singh, David Gomez, Sandeep Kedukodi and Ranjana Sandeep for the much needed fun times. Great appreciation to the HEFT Lab personnel, past and present, Dr. Justin Lamont, Dr. Arnab Roy, Dr. Colin Reagle, Sakshi Jain, Li Yang, Krishnashis Chatterjee, Dr. Ting Ma, Hardik Patel, Siddhartha Gadiraju, Bharath Vishwanathan and Samruddhi Deshpande, for helping me in their capacity during my time in the HEFT Lab. I would also like to thank Diana Israel for her extremely quick administrative skills and the Mechanical Engineering Machine Shop personnel for doing a great job in manufacturing test sections.

Through many years at Virginia Tech, the support of my friends has always been a motivating factor. Arijeet, Arijita, Aditya, Ambuj, Karthik, Kaushik and Yagnesh, thank

you for being there in the initial tough times. I would also like to thank Naveen and Arka for some good music and interesting conversations. You have all been a tremendous group of friends that I will cherish for life.

Things would have been very difficult without you Aakshita. Thank you for your help and support through the thick and thin of my journey. I could not have asked for better people to look up to than my brother Kshitiz and his wife, Ankita. Bhaiya and Bhabhi, you two inspire me to become the best I can be. Finally, I would not have been here without my parents, Sunita and Somender Tyagi, and their encouragement and guidance through my endeavors. Everything that I have achieved is the culmination of your tireless efforts and immense love. Thank you for everything.

Table of Contents

Abstract.....	ii
Acknowledgements	iv
Table of Contents	vi
List of Figures	viii
List of Tables	xii
1. Introduction.....	1
2. Literature Survey.....	8
2.1. Dimples	8
2.2. Impingement	11
2.3. Rib Turbulators.....	14
3. Test Rigs Used for Heat Transfer Measurements	17
3.1. Stationary Heat Transfer Rig	17
3.2. Rotating Heat Transfer Rig	19
4. Thermochromic Liquid Crystal Thermography.....	23
4.1. History of Thermochromic Liquid Crystals.....	25
4.2. The Semi – Infinite Solid Equation for Convective Boundary Conditions	26
4.3. Design of TLC Experiments	28
4.3.1. Test Section Design	28
4.3.2. Lighting Setup.....	30
4.3.3. Choosing a TLC Band	31
4.4. Data Reduction Technique.....	32
4.4.1. Calibration of TLC	32
4.4.2. Green-start Technique.....	34
4.5. Uncertainty Analysis	35
5. High Aspect Ratio Channel Featuring Different Dimple Configurations	37
5.1. Description of test-section	37
5.1.1. Mainstream Channel Dimensions.....	38
5.1.2. Dimple Configurations	38

5.1.3.	Numerical Simulations	41
5.2.	Results and Discussion	43
5.2.1.	Baseline (un-augmented) Case – Flat Plate	44
5.2.2.	Diamond shaped dimples	46
5.2.3.	Square shaped dimples.....	48
5.2.4.	Triangular Shaped Dimples	49
5.2.5.	Cylindrical Shaped Dimples	50
5.2.6.	Heat Transfer on Dimple End Walls	52
5.2.7.	Heat Transfer Behavior on the Side Walls.....	56
5.2.8.	Thermal – Hydraulic Performance of the Dimples	58
5.3.	Uncertainty Analysis	59
5.4.	Conclusion	60
6.	Rotating Two-Pass Channel with Impingement under High Reynolds Number	62
6.1.	Test Section Geometry.....	62
6.2.	Testing Procedures	63
6.3.	Experiment Validation.....	65
6.4.	Experiment Results and Discussion	66
6.4.1.	Heat Transfer Results for Stationary Tests	67
6.4.2.	Heat Transfer Results for Rotation Tests.....	71
6.5.	Experimental Uncertainty and Repeatability	72
6.6.	Comparison with a Traditional Ribbed Cooling Channel.....	73
6.7.	Conclusion	75
7.	Research Conclusion	76
	Nomenclature	78
	References.....	80

List of Figures

Figure 1. A Siemens SGT5-8000H gas turbine schematic showing the hot gas path temperature and typical blade temperature, from http://www.siemens.com/press/photo/EFPG20061001-01e , Used under fair use, 2015	2
Figure 2. Increase in maximum allowable temperature limit of turbine blades over the years, from http://www.virginia.edu/ms/research/wadley/high-temp.html , Used under fair use, 2015	2
Figure 3. Blade cooling features used in internal cooling, Han, J. C., and Rallabandi, A. P., 2010, “Turbine Blade Film Cooling Using PSP Technique,” <i>Front. Heat Mass Transf.</i> , 1(1). Used under fair use, 2015	4
Figure 4. Coriolis acceleration direction in reference to the rotational velocity and flow velocity	6
Figure 5. Flow across a dimple that shows two vortex pairs and a primary core, Han, J., and Wright, L. M., 2007, “Enhanced Internal Cooling of Turbine Blades and Vanes” <i>The Gas Turbine Handbook</i> , U.S.DOE, National Energy Technology Laboratory, Morgantown, WV, pp.321.”, Used under fair use, 2015	9
Figure 6. Rib placement parameters, where P is the pitch, e is rib height and H is the channel height	14
Figure 7. 90° ribs placed in a two-pass channel with a sharp U-bend, as used by Lamont et al. [37], Lamont, J. A., Ekkad, S. V., and Alvin, M. A., 2012, “Detailed Heat Transfer Measurements Inside Rotating Ribbed Channels Using the Transient Liquid Crystal Technique,” <i>J. Therm. Sci. Eng. Appl.</i> , 4(1), p. 011002, Used under fair use, 2015	15
Figure 8. Schematic of the Stationary Heat Transfer Rig showing various flow control and flow conditioning components.....	17
Figure 9. Test section input temperature response to the heated air	19
Figure 10. CAD Drawing of the Rotating Heat Transfer Rig from Lamont et al. [49], Lamont, J. a, Roy, C. J., and Stern, C. H., 2012, “Heat Transfer in Stationary and Rotating Coolant Channels Using a Transient Liquid Crystal Technique Heat Transfer in Stationary	

and Rotating Coolant Channels Using a Transient Liquid Crystal Technique”, Used under fair use, 2015..... 20

Figure 11. Rotating heat transfer rig showing the air supply system and the test section mounting details 22

Figure 12. TLC color change as temperature is increased. If temperature is decreased (fluid getting hot), same colors are reflected, with same accuracy and response time [51], Hallcrest, TLC Products for Use in Research and Testing Applications, Used under fair use, 2015..... 26

Figure 13. Semi – infinite solid with a convective boundary condition and temperature profile in the solid as time increases [52], Incropera, F. P., DeWitt, D. P., Bergman, T. L., and Lavine, A. S., 2007, Fundamentals of Heat and Mass Transfer, John Wiley & Sons, Used under fair use, 2015 27

Figure 14. Two ways to record color change in TLCs using a CCD camera 29

Figure 15. Lighting setup for the stationary heat transfer tests..... 31

Figure 16. Calibration setup indicating surface thermocouple and calibration region 33

Figure 17. Results of the calibration test run for green color to surface temperature 34

Figure 18. Mainstream channel shape and dimensions 38

Figure 19. Baseline (un-augmented) case..... 39

Figure 20. Dimple geometries tested, where A). Diamond, B). Square, C). Triangular and D). Cylindrical 40

Figure 21. Cross section of the dimples: A). Diamond, B). Square, C). Triangular and D). Cylindrical 41

Figure 22. Dimple plate region chosen for numerical simulations 42

Figure 23. Meshing of the CFD region 43

Figure 24. Nusselt number distribution for $Re = 21,000$ case for the flat plate 44

Figure 25. Spanwise averaged streamwise variation of Nu number for the baseline case for all three Reynolds numbers..... 45

Figure 26. Detailed normalized Nu number plot for diamond dimples for all three Reynolds numbers47

Figure 27. Spanwise averaged streamwise variation of Nu number for diamond dimple case for all three Reynolds numbers47

Figure 28. Detailed normalized Nu Number plot for square dimples for all three Reynolds numbers48

Figure 29. Spanwise averaged streamwise variation of Nu number for square dimple case for all three Reynolds numbers49

Figure 30. Detailed normalized Nu number plot for the triangular dimples for all three Reynolds numbers50

Figure 31. Spanwise averaged streamwise variation of Nu number for triangular dimple case for all three Reynolds numbers50

Figure 32. Detailed normalized Nu number plot for cylindrical dimples for all three Reynolds numbers51

Figure 33. Spanwise averaged streamwise variation of Nu number for cylindrical dimples for all three Reynolds numbers51

Figure 34. Detailed Nu number contours on diamond dimple end wall52

Figure 35. Air flow mechanism inside diamond dimples for $Re = 10,000$ case53

Figure 36. Detailed Nu number contours on square dimple end wall and flow streamlines showing air flow mechanism at for $Re = 10,000$ case54

Figure 37. Detailed Nu number contours on triangular dimple end wall and flow streamlines showing air flow mechanism55

Figure 38. Detailed Nu number contours on cylindrical dimple end wall and flow streamlines showing air flow mechanism56

Figure 39. Nu number distribution on side wall of cylindrical dimples at $Re = 21,000$...57

Figure 40. Air recirculation when viewed from the top57

Figure 41. Nu number distribution on side wall of square dimples at $Re = 21,000$ 58

Figure 42. Definition of geometrical parameters of tested model under rotating conditions 63

Figure 43. Color change of the target surface during liquid crystal tests 65

Figure 44. Comparison of Nu number between the present study and Pamula et al. [55], Pamula, G., Ekkad, S. V., and Acharya, S., 2000, “Influence of Crossflow-Induced Swirl and Impingement on Heat Transfer in a Two-Pass Channel Connected by Two Rows of Holes,” J. Heat Transfer, 122(2), pp. 587–597, Used under fair use, 2015..... 66

Figure 45. Detailed normalized Nu number plot for the Re=25,000 case at three rotation numbers 68

Figure 46. Normalized Nu number plot for Re=50,000 case 68

Figure 47. Nu number contours for the Re=75,000 case at three rotation numbers 69

Figure 48. Nu number contours for the Re=100,000 case at three rotation numbers 69

Figure 49. Streamwise variation of spanwise averaged normalized Nu number for the first pass plenum channel and second pass impingement channel under stationary and rotating conditions..... 70

Figure 50. Repeatability of transient liquid crystal measurement in this study 73

Figure 51. Comparison of the impingement study with Wagner’s ribbed and smooth channel..... 74

List of Tables

Table 1. Dimensions of the flat plate shown in Figure 19.....	39
Table 2. Dimensions of the dimple configurations shown in Figure 20	40
Table 3. t_{\max} for each case calculated using Equation (11).....	41
Table 4. Comparison of area-averaged Nu number values for flat plate with Dittus – Boelter correlation value	46
Table 5. Pressure drop for all five dimple geometries analyzed in this study	58
Table 6. Average Nu number ratio, pressure drop ratio, and thermal – hydraulic performance factor for all four dimple geometries	59
Table 7. Uncertainty in Nu number for $Re = 21,000$ case.....	60
Table 8. Dimensional and conditional parameters of the test section	64

1. Introduction

The focus of this thesis is on augmenting heat transfer in internal cooling channels which are used inside gas turbine blades, electric generator coils, cylinder linings of internal combustion engines and any other application where augmentation in heat transfer is required. Thermal management inside the turbine blades of a gas turbine is critical to allow long operating hours without failure. Typical turbine rotor inlet temperature in modern gas turbine engines can be up to 1400°C (Figure 1), which is much higher than the allowable metal temperatures of turbine blades, typically around 900°C (Figure 2). This large temperature differential, coupled with increased thermal stress due to high speed rotation, makes effective cooling, imperative. The air bled off from the compressor discharge is used for various cooling schemes in turbine sections, such as internal cooling, film cooling, disc cavity cooling, mate-face gap cooling etc. This coolant air imparts a direct penalty to the overall efficiency of the gas turbine engine. Therefore, much research has been carried out focused towards efficient cooling, i.e. maximum cooling with minimum usage of coolant.

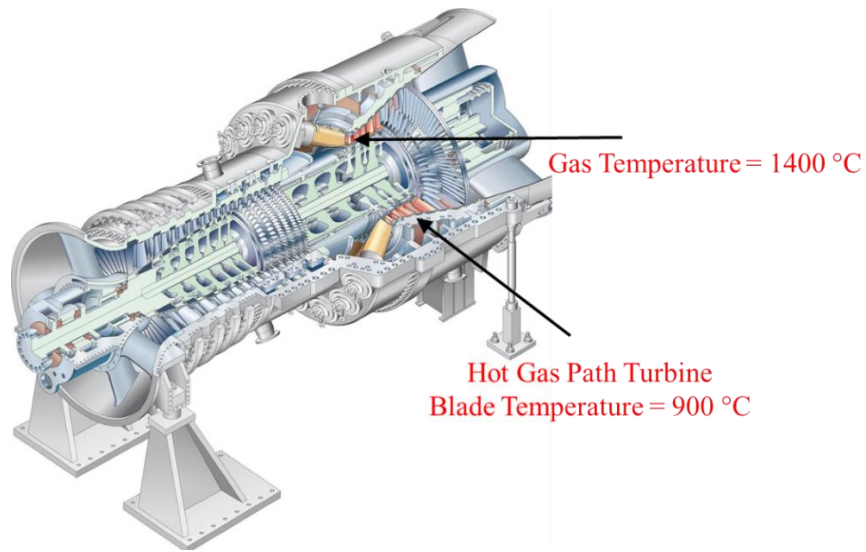


Figure 1. A Siemens SGT5-8000H gas turbine schematic showing the hot gas path temperature and typical blade temperature, from <http://www.siemens.com/press/photo/EFG20061001-01e>, Used under fair use, 2015

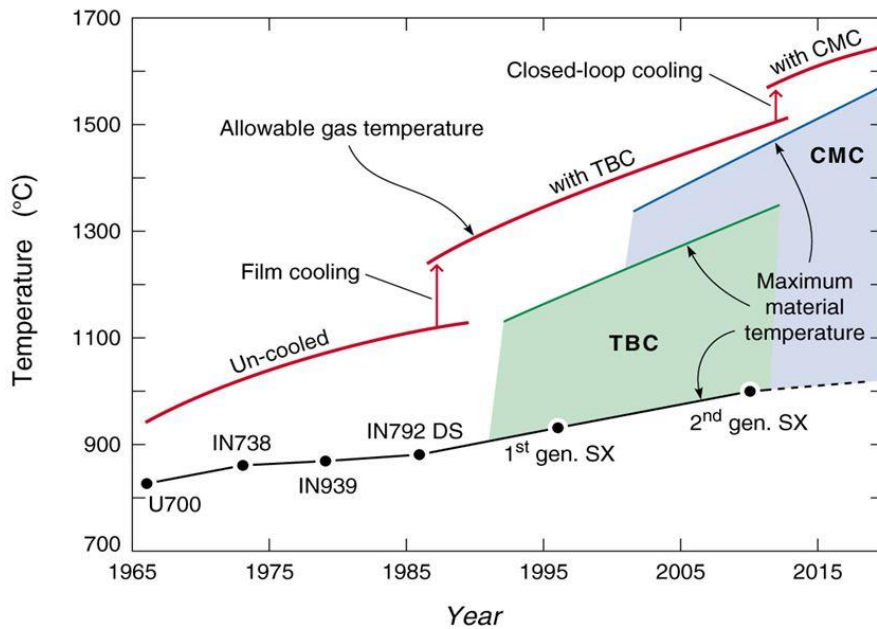


Figure 2. Increase in maximum allowable temperature limit of turbine blades over the years, from <http://www.virginia.edu/ms/research/wadley/high-temp.html>, Used under fair use, 2015

Enhancing the heat transfer in the internal channels of turbine blades can be done either by increasing the flow, using a different coolant type or by increasing turbulent mixing. Usually, coolant to the blades is drawn from the high pressure compressor stage of the engine and to maintain high thermal efficiency, only a limited amount of coolant can be extracted (about 15% to 20%). It is not feasible to use a different type of coolant, which would be supplied from outside the engine, due to the inherently complex design of the engines. Thus, one option to augment heat transfer is by using turbulent enhancers that increase the overall heat transfer coefficient. Many turbulence promoters, as shown in Figure 3, like jet impingement, rib turbulators, pin fin arrays and dimples are used. Each of these enhancement features have a unique set of advantages and disadvantages. Jet impingement provides one of the highest local heat transfer coefficients, but is susceptible to cross flow effects and rotation. Rib turbulators provide a relatively higher augmentation in heat transfer, but also have high friction factors resulting in increased use of coolant. Dimples are somewhat new in this field and have the advantage of low pressure drop penalties, but are still in the development phase of gas turbine cooling. Pin fins have been used extensively in the trailing edge cooling of blades as they provide structural strength, higher convectional cooling and improve conduction between the leading and trailing side, which reduces thermal stress gradients in the blade. However, pin fins have a high pressure drop penalty. Thus, a single cooling scheme is not used for the entire blade. Jet impingement is used in the blade leading edge region to alleviate local hot spots due to flow stagnation. Rib turbulators, on the other hand, are used in the serpentine channels and pin fins are used in the trailing edge region of the blade.

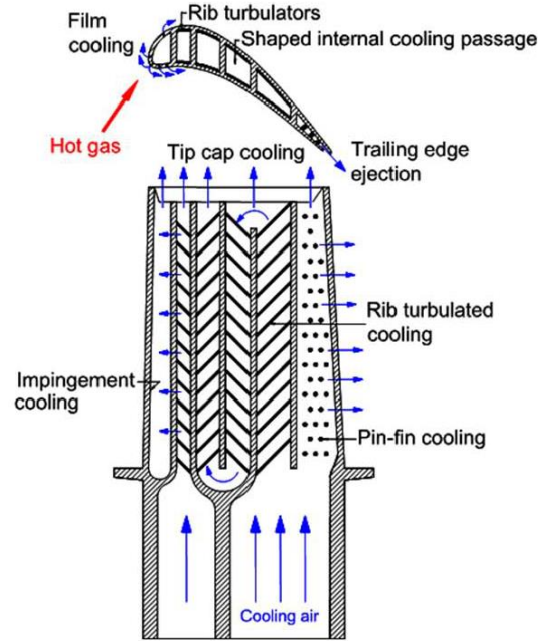


Figure 3. Blade cooling features used in internal cooling, Han, J. C., and Rallabandi, A. P., 2010, “Turbine Blade Film Cooling Using PSP Technique,” *Front. Heat Mass Transf.*, 1(1). Used under fair use, 2015

As described before, the penalty of using turbulence enhancing features is pressure loss in the channels. Thus each enhancing feature should be evaluated for thermal as well as its hydraulic performance. Such a performance factor is defined below as:

$$\eta = \frac{Nu/Nu_0}{(\Delta p/\Delta p_0)^{1/3}} \quad (1)$$

where, η is the thermal-hydraulic performance factor, Nu is the average Nusselt number of the enhanced channel, Nu_0 is the average Nusselt number of the unenhanced channel (usually smooth channel), Δp is the pressure drop in enhanced channel and Δp_0 is the pressure drop for the smooth channel. The normalized heat transfer coefficient, nusselt number (Nu), is defined as:

$$Nu = \frac{hD_h}{k_f} \quad (2)$$

where, h is the heat transfer coefficient, k_f is the thermal conductivity of the cooling fluid and D_h is the hydraulic diameter of the channel. A thermal-hydraulic performance factor greater than one implies that the performance of enhancing features is better than the smooth channel and less than one means vice versa.

Coolant channels under rotation are subjected to additional phenomena, Coriolis Effect and rotational buoyancy. The Coriolis acceleration is defined as:

$$\vec{a}_c = -2\vec{\omega} \times \vec{V} \quad (3)$$

where, $\vec{\omega}$ is the rotational velocity vector and \vec{V} is the flow velocity vector. The Coriolis acceleration originates due to the inertia of a particle to move in the direction of velocity vector, but is caused to deviate due to the rotational velocity of the system. Since the Coriolis acceleration is a resultant of a vector product between the rotational velocity and the flow velocity, its direction can change with the change in direction in either of its constituting vectors. Figure 4 explains this through a schematic. Flow going radially outward experiences Coriolis acceleration out of the page, whereas flow going radially inward experiences it into the page.

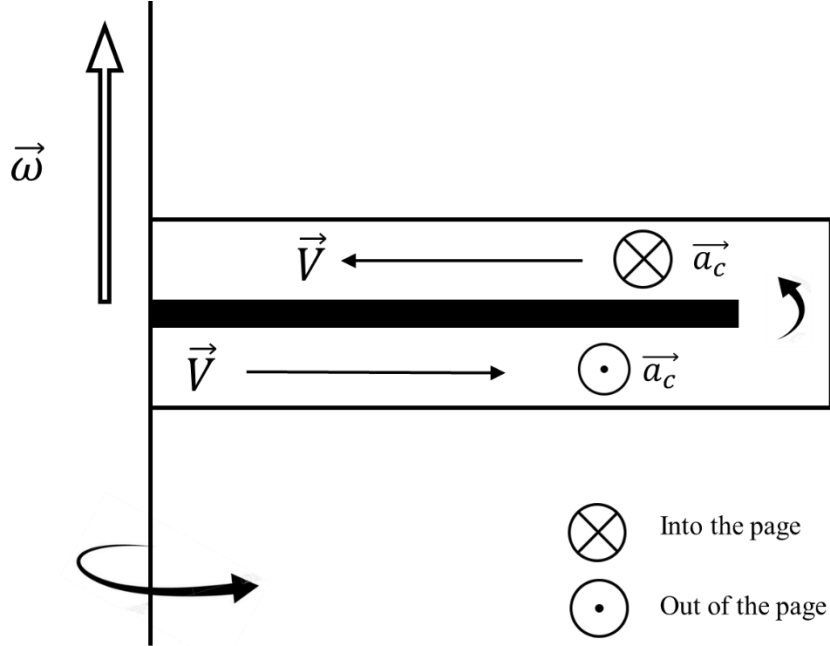


Figure 4. Coriolis acceleration direction in reference to the rotational velocity and flow velocity

The rotational buoyancy is the second phenomenon that affects flow in an internal channel. It is caused due to large temperature differences between the air near the surface and the air in the core flow. To determine whether this phenomenon is prominent, the Grashof number is calculated which is given as:

$$Gr_{D_h} = \frac{g\beta(T_w - T_m)D_h^3}{\nu^2} \quad (4)$$

where, Gr_{D_h} is the Grashof number, g is acceleration due to gravity, β is the volumetric thermal expansion coefficient, T_w is the wall temperature, T_m is the bulk temperature, and ν is the kinematic viscosity of the fluid. Since the Grashof number describes the relative importance of buoyancy driven forces to viscous forces, in a rotating frame, acceleration due to gravity (natural convection) is not as important and is replaced by $\omega^2 R$, where R is the distance to the axis of rotation. When this is done, a non-dimensional buoyancy parameter can be defined as:

$$BP = \frac{\Delta\rho}{\rho} \frac{R_m}{D_h} Ro^2 \quad (5)$$

where, BP is the buoyancy parameter, $\Delta\rho/\rho$ is the coolant-to-wall density ratio (DR), R_m is the mean rotating radius and Ro is the rotation number, defined as:

$$Ro = \frac{\omega D_h}{V} \quad (6)$$

where, V is the velocity of the coolant at the channel inlet. The buoyancy parameter changes with the rotation number, however the density ratio is relatively constant. During experiments in a lab environment, the density ratio is also kept constant to simulate the real conditions.

The focus of this research was to evaluate various internal cooling schemes like dimples and impingement. As discussed in the literature review section, not much is known about heat transfer on the walls of a dimple and an attempt was made to understand flow behavior inside dimples of various shapes. Also, a two-pass-channel with swirl induced impingement was studied that may reduce the effect of rotation on heat transfer distribution in the channels.

2. Literature Survey

With the ever increasing demand of high thermal efficiency gas turbine engines, turbine inlet temperatures have increased significantly over the years. Higher turbine inlet temperatures have the potential to reduce the life of turbine components or even result in permanent damage, thus making the effective cooling of the same, imperative.

Over the years, several techniques have been employed to gas turbine blade internals to enhance the heat transfer rate due to convection, such as, dimpled surfaces, jet impingement, rib turbulators, and pin fins etc. A completed review of internal cooling technologies can be found in the book by Han et al. [2]. A brief overview of the available literature of these cooling techniques is given below.

2.1. Dimples

It has been proven that dimples have better performance as compared to the rib turbulators, however much research has to be carried out towards the optimization of dimple shapes, so as to promote them to a stage where they can replace rib turbulators. Dimple impose a lower pressure drop penalty as compared to ribs, as they do not block the flow passage thereby resulting in minimal pressure loss, and thus can be employed in later turbine stages. Additionally, the vortex pairs produced by dimples are transported by the flow further downstream, thus resulting in heat transfer enhancement [3]. This is explained by Figure 5. The primary upwash of the flow exiting the dimple advects heat from the dimple to the cold mainstream flow above the dimple [4].

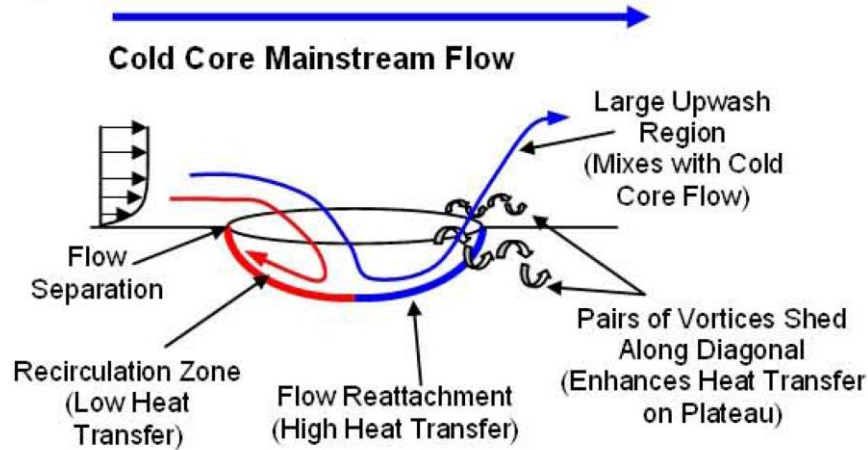


Figure 5. Flow across a dimple that shows two vortex pairs and a primary core, Han, J., and Wright, L. M., 2007, “Enhanced Internal Cooling of Turbine Blades and Vanes”*The Gas Turbine Handbook*, U.S.DOE, National Energy Technology Laboratory, Morgantown, WV, pp.321.”, Used under fair use, 2015

The effect of dimple depth on heat transfer enhancement has been studied by Burgess et al. [5], where the authors proposed that increase in dimple depth, leads to increment in the intensity of vortices and the secondary flows associated with the dimples as well as an increment in the 3-D turbulence and its transport downstream of dimples, thus resulting in higher heat transfer enhancement. Ligrani et al. [6,7] studied flow structures generated due to dimpled geometries and their transport in the streamwise direction. They found that, with the decreasing value of the channel height to dimple print diameter ratio, the strength of the primary vortex increases and that the location of these vortices lies in close proximity to areas where the augmentation in normalized Reynolds normal stress was observed. These studies hinted in a possible relation between the vortices, Reynolds normal stress and mixing of the flow over dimpled geometries. Won et al. [8] studied the effects of dimple depths on the flow structure over a channel. The authors reported that dimples with

greater depths produced vortices, which were bigger and possessed increased intensity, as well as had increased turbulent transport capacities. Slabaugh et al. [9] studied the performance of a dimpled surface aligned in two columns. The authors reported that the channel-averaged Nusselt number improved by as much as sixty percent with the use of double-dimpled surface as compared to smooth wall dimples. Acharya et al. [10] carried out experimental (naphthalene sublimation method) and computational (FLUENT) investigations on the effects of different dimple shapes on the heat transfer enhancement. The authors reported the flow patterns and heat transfer distributions for four dimple configurations, square, triangular, circular and teardrop and concluded that the teardrop dimple has the highest transfer among the four configurations listed above. The study also gave explanation, based on numerical techniques, as to how heat transfer occurs on the walls of the dimples.

Moon et al. [11] studied the effect of channel height on the heat transfer enhancement due to imprinted dimple features. They carried out experiments for a range of relative channel height values (0.37 to 1.49), and found out that the distribution of heat transfer coefficient was more or less unaffected with the variation in relative channel height values and similar trends were observed for the friction factor as well. Shin et al. [12] studied the effects of the arrangement of dimples and channel height on the heat transfer coefficient. The authors reported results which showed relatively higher heat transfer coefficients downstream of the dimples due to flow reattachment, when compared to the area upstream of the dimple where flow recirculation resulted in comparably lower heat transfer coefficient. Hwang et al. [13] studied the effects of dimples and protrusions in a rectangular duct by carrying out experiments at a relatively lower Reynolds number range. The authors

assessed that for the double dimple wall and double protrusion wall cases, the heat transfer enhancement (as compared with the smooth plate) levels were higher for lower Reynolds number as compared to higher Reynolds number. Lamont et al. [14] studied the effect of dimple depth in a narrow diverging channel and suggested an optimum value of diameter to depth ratio of 3 to 5. Ekkad et al. [15] studied the effects of dimpled surface in high aspect ratio channels for a wide range of Reynolds number and observed that the heat transfer enhancement was as high as three times as compared to that of a flat plate. Ekkad et al. [16] studied the performance of a dimpled target surface with the jet impingement heat transfer enhancement technique. The author stated that, dimple configurations, both in-line and staggered, produced lower heat transfer coefficients as compared to the non-dimpled target surface.

All of the aforementioned studies focus on the effect generated by the dimples in the mainstream flow, but there is little information available as to how heat transfer occurs on the dimple walls. In addition, there are no studies that go towards a high aspect ratio channel geometry which can be found in the trailing edge of a turbine blade.

2.2. Impingement

Based on the findings of Han et al. [2], impingement is one of the most effective cooling technology, which is not only used in gas turbine industry, but other areas like electronic chip cooling and heat exchanger systems. Han and Goldstein [17] and Viskanta et al. [18] summarized investigations prior to 2001. Numerous studies on single jet, inclined single array jets and multiple array jets were included in their review. Correlations for both heat transfer and pressure drop were derived. Recent investigations prior to 2005

can be found in Zukerman and Lior's [19] review paper. Experimental data including stagnation point and spatially-averaged surface heat transfer coefficients were summarized with a Reynolds number ranging from 1,500 to 400,000. Recent studies by Ricklick et al. [20–22] investigated the influence of channel height, jet space and bulk temperature on a single inline row of impinging jets. The choice of bulk temperature is important to determine the heat transfer coefficient and avoid large error. Detailed wall flow topology was shown for both single jet and showerhead jets. Impingement cooling on rib-roughed leading edge surface was also investigated by Taslim et al. [23–25]. Notched-horseshoe ribs produced the highest heat removal from the target surface, which was attributed entirely to the area increase of the target surface. Numerical studies were also summarised by Zukerman and Lior [19] and Ibrahim et al.[26]. The SST turbulence model was considered as an effective model among all the two equation models.

An earlier study by Parsons et al. [27] focused on a radially outward channel with a single array of impinging jets on both sides. The jet Reynolds number was 10,000 and the rotation number was 0.0028. Heat transfer on all sides of the channel decreased up to 20 percent compared to those results that correspond to non-rotating conditions. Detailed measurement of the flow field and Nusselt number distribution have been carried out by Kreatsoulas et al. [28,29]. An IR camera was used for the heat transfer measurement. A decrease in the averaged Nusselt number by up to 30 percent was observed at high rotation speeds. A series of correlations for Nusselt number were derived with a formula including rotation number, Reynolds number and Rayleigh number. The effect of rotation on jet impingement in blade leading edge was measured by Elston and Wright [30,31]. The jet Reynolds numbers ranged from 10,300 to 41,000 with rotation numbers varying up to 1.0,

and buoyancy numbers exceeding 4.0. Results indicated that the degree of separation between the leading and trailing surface increased with increasing rotation number. The deflection of the impinging jet combined with rotation induced by secondary flows offered increased mixing within the impingement cavity and enhanced heat transfer. Leading edge impingement with and without film cooling holes were measured by Hong et al. [32–34] under rotating conditions. The jet Reynolds number ranged from 3,000 to 5,000 with rotation numbers up to 0.0075. During rotation, asymmetric heat transfer distribution was observed on the target surface. However, the averaged value was not substantially influenced by rotation. The rotation effect was found to be different with different jet to target distances. Li and Chiang [35] compared the cooling performance of ribbed channels and impingement channels under rotating conditions. Reynolds numbers ranged from 10,000 to 30,000 and rotation numbers were up to 0.079. Results indicated a local heat transfer enhancement in ribbed channels and a local reduction of heat transfer in impingement channels. PIV and LDA measurements were utilized in rotating impingement experiment by Iacovides et al. [36]. A single array of jets with Reynolds number of 15,000 and a rotation number of 0.18 was studied. Rotation led to the disappearance of all secondary peaks and also some of the primary peaks of impingement. Rotation increased the spreading rate of the jets and reduced the heat transfer. Recent studies by Lamont et al. [37–39] presented rotation results of both single array and double array jet impingement. The measurement employs the transient liquid crystal (TLC) technique. Similar phenomenon with serpentine ribbed channels was observed in channels with impingement. The trailing side experiences an increase in heat transfer and the leading side experiences

a decrease for all jet channel height to jet diameter ratios. However, the change caused by rotation is not as significant as that in ribbed channels.

2.3. Rib Turbulators

Use of periodic rib turbulators is very popular in enhancing heat transfer in internal passages. These rib turbulators trip the boundary layer and enhance mixing, thus enhancing the overall heat transfer with a penalty of a pressure drop which is overcome by the level of heat transfer enhancement. Many parameters about these turbulators like shape, height and pitch, as shown in Figure 6 can be varied and as expected, many studies over the years have played around with these parameters to achieve the most optimum shape.

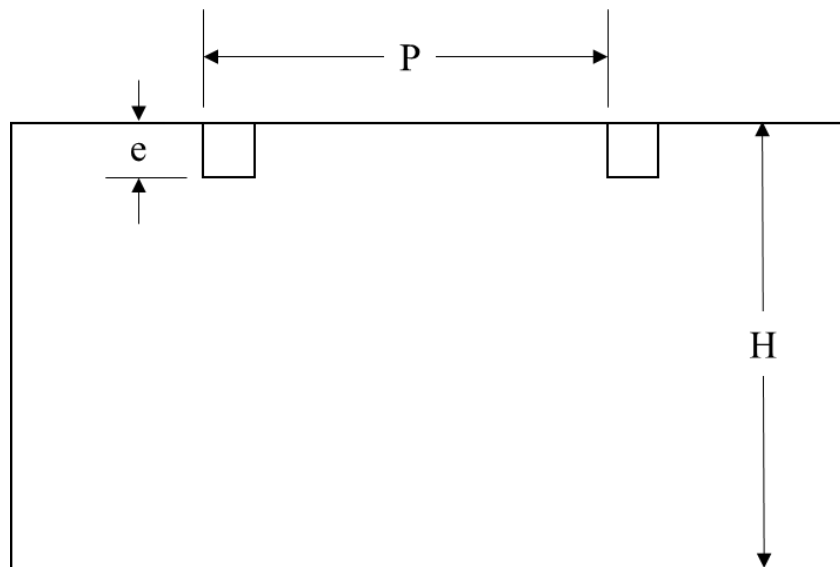


Figure 6. Rib placement parameters, where P is the pitch, e is rib height and H is the channel height

The usage of ribs in actual gas turbine cooling passages is also dependent on ease of manufacturing the complex shapes into blades. Thus, the most commonly studied and used

rib type are 90° ribs which are orthogonal to the flow direction, as shown in Figure 7 and are easiest to manufacture in blade passages.

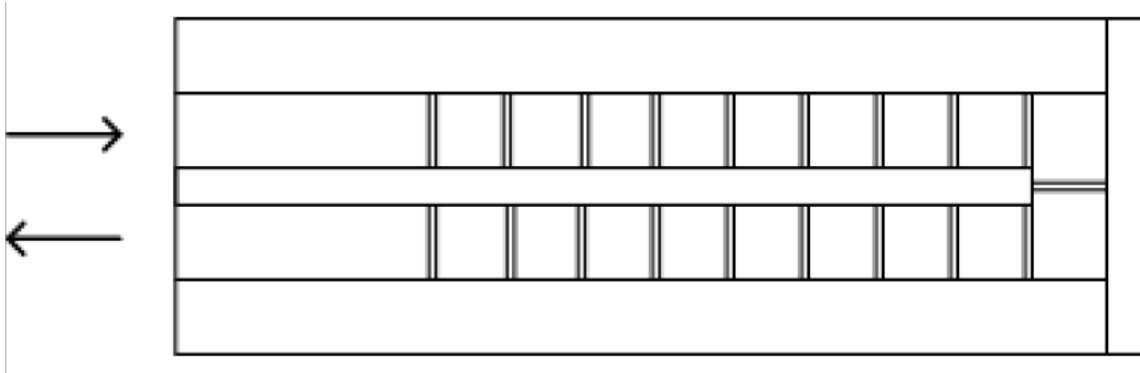


Figure 7. 90° ribs placed in a two-pass channel with a sharp U-bend, as used by Lamont et al. [37], Lamont, J. A., Ekkad, S. V., and Alvin, M. A., 2012, “Detailed Heat Transfer Measurements Inside Rotating Ribbed Channels Using the Transient Liquid Crystal Technique,” *J. Therm. Sci. Eng. Appl.*, 4(1), p. 011002, Used under fair use, 2015

The first detailed heat transfer coefficients in rib turbulated channels was given by Han [40], in which optimum geometry was identified and correlations for heat transfer prediction were prescribed. Wagner et al. [41] studied 90° ribs in a rotating multi-pass channel where an increase in enhancement was observed in the trailing side of the first pass and a decrease in the leading side. In the second pass, however, the trailing side shows a decrease in enhancement and leading side experiences higher heat transfer, which is opposite of the first pass. The average heat transfer values were reported to be higher than the smooth wall case. Taslim et al. [42] investigated 90° ribs with rotation and varied the rib blockage ratio (e/H rib height to channel height ratio). With a higher blockage ratio, higher heat transfer was observed.

Over the years, angled ribs have also gained prominence because they achieve higher heat transfer. Angled ribs, unlike 90° ribs, can impart swirl to the flow and produce

secondary flow vortices that mix the hot air near the surface with the cold core flow. Zhang et al. [43] studied 60° ribs and found that for stationary and rotating cases, 60° ribs perform better than smooth channel. Johnson et al. [44] compared 45° ribs to 90° ribs and found that 45° ribs outperform the 90° ribs. To further increase heat transfer by increasing swirl in the flow, complex shaped ribs with multiple angled ribs were tested. Some of the rib turbulators' configuration and shapes studied in both stationary and rotating frame of references are 90-deg continuous rib, 90-deg broken rib, 60-deg parallel broken rib, 45-deg parallel broken rib, 60-deg V-shaped broken rib, 45-deg V-shaped broken rib, 60-deg parallel continuous rib, 45-deg parallel continuous rib, 60-deg V-parallel continuous rib, 45-deg V-parallel continuous rib, inverted parallel V-shaped, inverted discrete V-shaped, parallel V-shaped with gaps, parallel W-shaped rib, discrete W-shaped rib and many more [4]. Apart from experimental investigations on rib turbulated channels, several numerical studies have been carried out utilizing different turbulence models to study the flow phenomena and heat transfer [45–48].

3. Test Rigs Used for Heat Transfer Measurements

Experiments were performed on two heat transfer rigs, namely the stationary heat transfer rig and the rotating heat transfer rig. These rigs were designed with the primary aim of conducting heat transfer measurements while providing good flow control as well. Since liquid crystal thermography requires a clear visual access to the test section, access to cameras was also required. A brief discussion on both the rigs is given below.

3.1. Stationary Heat Transfer Rig

The experimental setup of the stationary heat transfer rig is shown in Figure 8. The working fluid (air) is supplied from a compressor (shop air), and the flow rate is controlled by a flow control valve, located upstream of the orifice plate ($L/d \sim 36$).

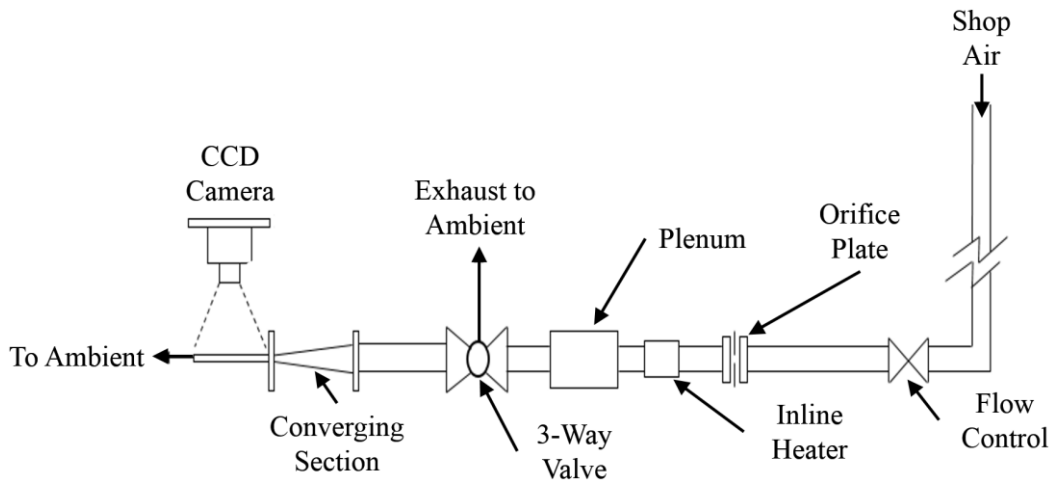


Figure 8. Schematic of the Stationary Heat Transfer Rig showing various flow control and flow conditioning components

For the measurement of flow rate, the compressibility effects of air including the density dependence on pressure of compressed air, has been taken into account. The inlet pressure is measured by a pressure transducer (Manuf.: Omega, part no. PX309-030G5V)

and the differential pressure across the orifice plate is measured by a differential pressure transducer (Manuf.: Omega, PX277-30D5V). A DC power supply is used to provide excitation voltage to the pressure transducers and the resulting signal is read by a LabVIEW VI which is also capable of recording pressure values in a text file. An in house computer program is used to determine the flow rate by using the two pressure measurements. Before the experiments are conducted, the heater (Manuf.: Sylvania, part no. Sureheat Jet, 8 kW, 760°C, 240 V, single phase) is turned on and the heated air is vented to the ambient through a 3-way ball valve until a steady temperature value of about 65°C is achieved. The heater is located about $L/d \sim 10$ downstream of the orifice plate so as to minimize the effect of the heater on flow measurements. The outlet temperature of the heater is controlled using a steady state relay provided by the manufacturer. Once a steady exhaust temperature is achieved, the three way valve is switched to the test section to set the flow rate. Once the desired flow rate is set, the valve is switched back to exhaust direction. The test section is allowed to cool down to room temperature (for about 1 hour) before conducting a transient test.

Figure 9 shows the typical response of the inlet thermocouple of the test section when the 3-way valve is switched and heated air is allowed to enter the test section. Such a step response is necessary for a transient test to induce color change in liquid crystal. Also, a key assumption for heat transfer coefficient estimation is that the mainstream temperature stays constant during the entire experiment time. Figure 9 shows an increasing trend which is due to the thermal inertia presented by the unheated walls of the converging section. As the walls heat up with time, the temperature recorded by the thermocouple increases. Since the typical test time is less than 30 seconds, the change in temperature, from the switch of

the valve to conclusion of test, is about 5°C and does not adversely affect the heat transfer results.

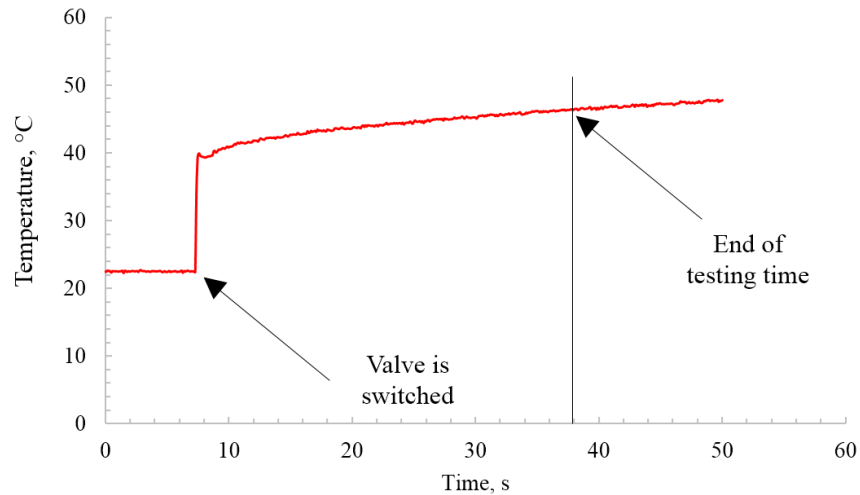


Figure 9. Test section input temperature response to the heated air

3.2. Rotating Heat Transfer Rig

To conduct transient liquid crystal experiments in a rotating frame, the rotating heat transfer rig was used. This rig, designed by Lamont [49] and shown in Figure 10, allows a camera to be mounted with the test section that can capture color change in the liquid crystals. A 3-phase motor (Manuf. Baldor, part no. EM3663T, 3475 rpm, 60 Hz, 5 hp) is used to rotate the test section. A timing belt allows the motor speed to be reduced by a factor of three, and hence the maximum possible rotation speed is about 1150 rpm for the rig. This reduction allows the stresses experienced by the rig to be within the design limit. A variable frequency drive (VFD) is used to control the rotational speed of the test section. A 2 inch diameter protrusion on the opposite side of the test section on the drive shaft allows standard counter weights to be added for balancing the rig. Large diameter steel washers are used as spacers between the counter weights to equalize the moments on the

drive shaft. The entire rig is bolted to the ground and vibration damping pads are used to nullify any vibrations reaching the floor.

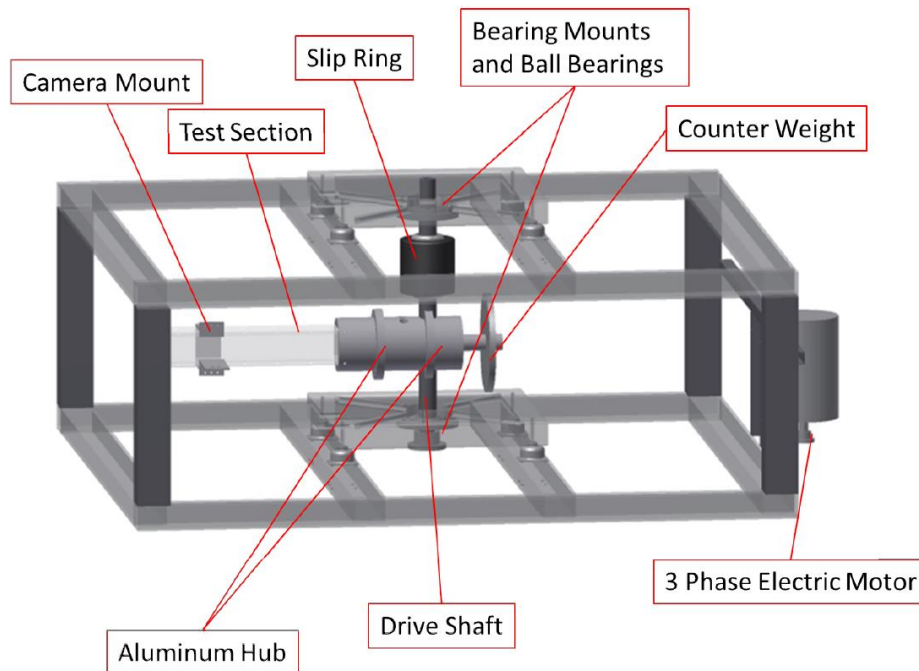


Figure 10. CAD Drawing of the Rotating Heat Transfer Rig from Lamont et al. [49], Lamont, J. a, Roy, C. J., and Stern, C. H., 2012, “Heat Transfer in Stationary and Rotating Coolant Channels Using a Transient Liquid Crystal Technique Heat Transfer in Stationary and Rotating Coolant Channels Using a Transient Liquid Crystal Technique”, Used under fair use, 2015

Air flow enters the rig through a rotary union into the drive shaft, which is bored out axially to 8 inches. Then, it is redirected into the test section where k-type thermocouples are used to measure the temperature change. The information from thermocouples is transmitted through the slip ring and out of the rig into a data acquisition system. A GoPro Hero 3+ Black Edition camera is mounted about 6 inches away from the test section using an aluminum frame. Due to high g forces experienced by the camera during rotational testing, the camera optics may move inside that would result in loss of video data. The

GoPro has fixed optics and has been designed for rough environments where delicate camera optics may get damaged. The GoPro also allows wireless control of the camera. Live feed from the GoPro is also monitored during test runs. LED lights are used to provide illumination to the test section. The LED strips are angled at 45° to reduce reflected light glare from the test section reaching the camera.

Figure 10 shows the flow conditioning system of the rotating heat transfer rig. To match the buoyancy driven force directions in a gas turbine blade, the coolant must get heated in the test section. There are two ways to achieve this: heat the test section walls or provide a lower than room temperature air. The instrumentation cost of creating a heated test section in a rotating frame would be immense. Plus, electrical power must be provided to the heating elements through the slip ring, which would drive the cost of the slip ring even more. It was also desirable to use the liquid crystal thermography technique as it provides detailed heat transfer data, and thus visual access to the walls of the test section is a must. Keeping these factors in mind, the second idea of providing chilled air to the test section was chosen. To do this, a liquid nitrogen and air mixture is used to chill the channel length leading to the test section. A thermocouple at the end of the channel is used to measure the venting air temperature. For different flow rates, the coolant channel must be cooled accordingly to achieve the same buoyancy parameter in the test section. It is to be noted that the test section walls remain at room temperature when the air flow channel is cooled using liquid nitrogen and air mixture. A 3-way ball valve is used to divert the liquid nitrogen and air mixture before the test section. Once the channel is cooled to the required temperature, liquid nitrogen flow is shut off and main air flow is vented before the chilled channel. Then using an orifice plate, differential and static pressure manometers, an

appropriate flow rate for the experiment is set. Since the pressure drop experienced by the air at the vent is lower than the pressure drop due to the test section, initial calibration runs are conducted. A test matrix is created where the relationship of vent pressure drop to test section pressure drop is established. This relationship is later used to set the appropriate flow rate before the chilled path that would result in the correct flow rate at the test section. The 3-way valve located before the test section is then switched to allow air entry into the test section. Then, using the VFD, the rotational speed is slowly increased. An infrared rpm indicator is used to monitor the rotational speed. Once the correct speed is reached, the test is commenced. A LabVIEW VI is used to record the temperatures inside the test section.

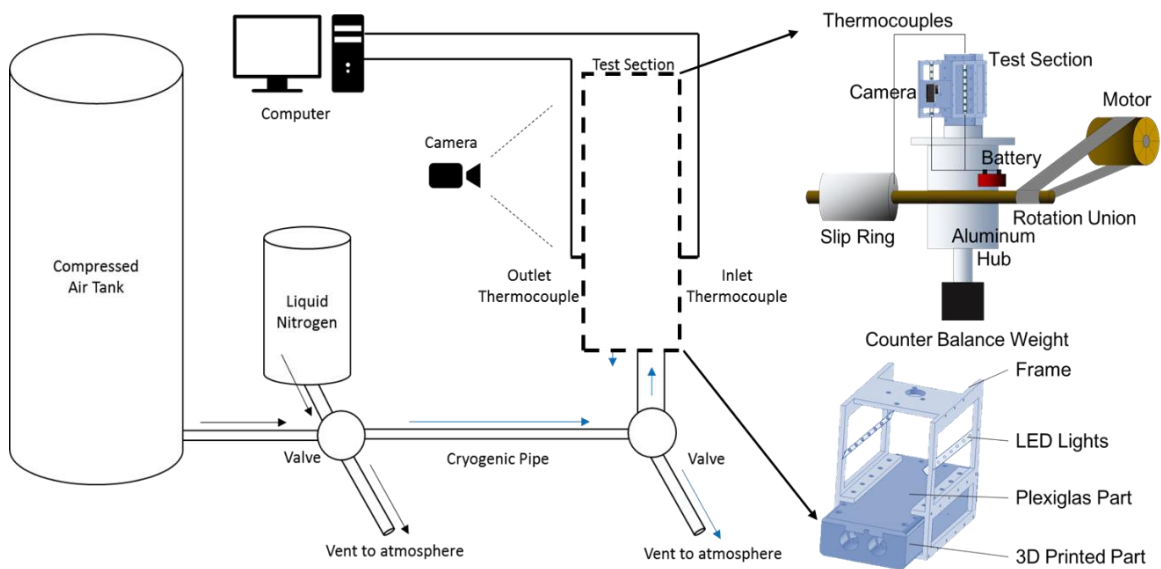


Figure 11. Rotating heat transfer rig showing the air supply system and the test section mounting details

4. Thermochromic Liquid Crystal Thermography

As heated air passes over a solid body's surface, it deposits heat on the surface which then diffuses into the solid. The heat transfer on the surface is dictated by Newton's law of cooling (or heating),

$$q = hA_s(T_m - T_w) \quad (7)$$

where, q is the heat energy deposited on the surface, h is the heat transfer coefficient, A_s is the surface area, T_m is the mainstream temperature of the air and T_w is the surface temperature. Usually, the heat flux form of this equation is used where Equation (7) is divided by the surface area. The heat transfer coefficient is a hydrodynamic property, i.e. it only depends on the physical properties of the fluid and the flow features like fluid velocity and surface geometrical features. Qualitatively, value of heat transfer coefficient determines how well heat is exchanged from the fluid to the solid body's surface. A large heat transfer coefficient would mean that heat exchange is rapid and a low value would mean vice versa. For laminar flow in internal channels, an analytical solution of the Navier – Stokes equations gives an exact relation for calculating heat transfer coefficient. However, no fundamental equation exists for turbulent flow that may calculate the heat transfer coefficient at a location based on the fluid properties at that location. The Dittus – Boelter correlation is the most widely used equation for estimating heat transfer coefficient in fully developed circular internal flows. It is given by

$$Nu = 0.023Re^{0.8}Pr^n \quad (8)$$

where, Re is the Reynolds number, Pr is the Prandtl number and n is 0.3 for cooling of the fluid and 0.4 for heating of the fluid. This equation, as stated before, is only valid for fully developed flows in circular internal channels. Also the Reynolds number should be greater

than 10,000 and the development length for the flow should be at least 10 times the hydraulic diameter. For extreme departures from the circular cross section, for example very high aspect ratio channels of greater than 10, Dittus – Boelter may not hold true either. Therefore, a difference of about $\pm 15\%$ in Nu number value should be expected. Thus, every geometry in a turbulent flow requires testing to determine, at the very least, the level of departure from the Dittus – Boelter correlation.

In essence, convection is a heat transfer phenomenon dictated by near surface physics like boundary layer theory, and hence knowledge of heat transfer near the surface will yield information about convective heat transfer. To do this, some measurable quantity must be chosen, which in this case would be the surface temperature. The change of surface temperature at a particular location with time can be related to the heat transfer at that location. In most engineering applications, heat transfer coefficient is an unknown value and various methods are utilized to estimate it. A simple thermocouple measurement at a point location can be used to estimate an area averaged value of heat transfer coefficient. For detailed and localized knowledge, few techniques exist. An infrared camera can be used to record surface temperature variation, but it is an expensive and bulky equipment to use, especially in a rotating environment. Some researchers have used a naphthalene sublimation technique where heat and mass transfer analogy is used to estimate the heat transfer coefficient. The test section is manufactured by depositing precise amounts of naphthalene on the surface. During experiment, as air passes over the surface, naphthalene sublimates into the air. After the experiment, the depletion in naphthalene layer is measured using surface profile meters. This technique gives localized results, however it is expensive, cumbersome and data reduction must be done immediately following the test

as naphthalene continuously sublimates into the ambient. The most practical choice is to use temperature sensitive liquid crystal paint as it is inexpensive and can be used in variety of applications, including rotating environments. The following sections present a brief overview of liquid crystals and the data measurement technique utilized in this study.

4.1. History of Thermochromic Liquid Crystals

Thermochromic Liquid Crystals (TLCs) were found in the 1880s, but their use in heat transfer study started in early 1970s. They exist as either cholesterics, chiral nematics or a combination of both. As described by Ekkad et al. [50], liquid crystals are called thermochromic because they reflect the incident white light with different color subject to temperature changes. TLCs can be manufactured to have temperature play anywhere from -30°C to 120°C with bandwidths between 1°C to 20°C [51]. A thin liquid crystal layer (about 10 microns thick) is colorless against a black background. As temperature increases, the liquid crystal molecules fold and unfold, and at a particular time instant, only a single wavelength of light is reflected, and the rest is transmitted to the molecule. The wavelength of reflected light is thus temperature dependent (shown in Figure 12). This is the fundamental relation which is used in convective heat transfer study. Many researchers have used this relationship over past three decades, in steady state and transient tests, to determine surface temperature profile over complex geometries. The present study utilizes a transient technique using the TLCs to map the time variation of surface temperature and relate it to the heat transfer coefficient.

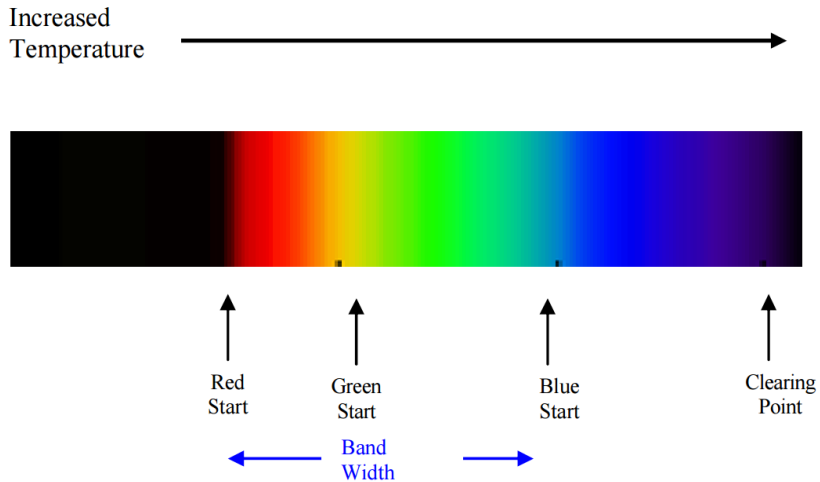


Figure 12. TLC color change as temperature is increased. If temperature is decreased (fluid getting hot), same colors are reflected, with same accuracy and response time [51], Hallcrest, TLC Products for Use in Research and Testing Applications, Used under fair use, 2015.

4.2. The Semi – Infinite Solid Equation for Convective Boundary Conditions

Heat transfer coefficient over a surface can be determined using the one dimensional formulation of the semi – infinite solid assumption. As shown in Figure 13, a solid with infinite thickness in x-direction is exposed to a convective boundary condition at its left edge. Assuming that the outside air is hotter than the solid, heat starts propagating in the solid and the temperature inside the solid increases with time.

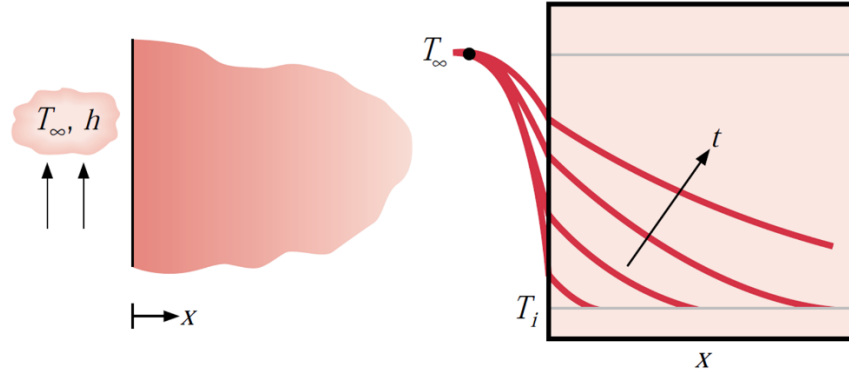


Figure 13. Semi – infinite solid with a convective boundary condition and temperature profile in the solid as time increases [52], Incropera, F. P., DeWitt, D. P., Bergman, T. L., and Lavine, A. S., 2007, Fundamentals of Heat and Mass Transfer, John Wiley & Sons, Used under fair use, 2015

Since a transient technique is to be used, the 1D transient conduction equation is given as:

$$k_s \frac{\partial^2 T}{\partial x^2} = \rho_s C_{p_s} \frac{\partial T}{\partial t} \quad (9)$$

where, T is the temperature inside the solid, x is the location inside the solid, k_s is the thermal conductivity of the solid, ρ_s is the density of the solid, C_{p_s} is the thermal capacity of the solid and t is the time. The initial and boundary conditions are defined as

$$\begin{aligned} @t = 0, \quad T_{(x,0)} &= T_i \\ @x = 0, \quad -k_s \left. \frac{\partial T}{\partial x} \right|_{x=0} &= h(T_\infty - T_{(0,t)}) \\ @x \rightarrow \infty, \quad T_{(x \rightarrow \infty, t)} &= T_i \end{aligned}$$

Where $T_{(x,0)}$ is the temperature of the solid at time equal to zero, T_i is the initial temperature value for the solid, T_∞ is the mainstream air temperature, $T_{(0,t)}$ is the surface temperature and $T_{(x \rightarrow \infty, t)}$ is the temperature at the infinite boundary. Solving Equation (9), with the prescribed initial and boundary conditions, we obtain a temperature distribution at the convective boundary surface (at $x = 0$) as (from Incropera and Dewitt [52]),

$$\frac{T_{(0,t)} - T_i}{T_\infty - T_i} = 1 - \exp\left(\frac{h^2 \alpha_s t}{k_s^2}\right) \operatorname{erfc}\left(\frac{h \sqrt{\alpha_s t}}{k_s}\right) \quad (10)$$

Where \exp is the exponential function, erfc is the complementary Gaussian error function and α_s is the thermal diffusivity of the solid. The critical assumptions for using Equation (10) are that the mainstream temperature, T_∞ , and the heat transfer coefficient are not time dependent. If these two quantities are time variant, then Equation (10) must be changed accordingly. In reality, the test surface thickness will be finite, and hence testing time must be limited to not violate the boundary condition at the other surface. A conservative estimate for the duration of a transient test is given by

$$t_{max} = 0.1 \frac{H^2}{\alpha_s} \quad (11)$$

Where t_{max} is the maximum time for a transient test and H is the thickness of the solid. The heat transfer coefficient cannot be solved for explicitly, thus an iterative solver (error minimization) is used. More details are given in the Data Reduction Technique subsection.

4.3. Design of TLC Experiments

Experiments must be designed with careful considerations to minimize measurement error. These considerations include test section design, choice of TLC band and understanding the test rig capabilities.

4.3.1. Test Section Design

As noted in previous section, Equation (10) is 1D in nature and does not consider 2D thermal conduction effects. To keep this thermal model valid during experiments, a low thermal conductivity material must be used to make the test section. In addition to that,

optical access is required to record the color change of the liquid crystals. Hence, clear acrylics are the natural choice for test section design. It has a thermal conductivity of 0.19 W/mK and a thermal diffusivity of $1.09 \cdot 10^{-7} \text{ m}^2/\text{s}$. For complex turbulence features, like dimples, pin fins and ribs etc., and for ease of manufacturability, 3D printing using ABS plastic is also used extensively. The additive manufacturing process prints the requested geometry in layers with a resolution of 0.187mm. Like clear acrylic, ABS has similar thermal properties ($k = 0.18 \text{ W/mK}$ and thermal diffusivity $1.2 \cdot 10^{-7} \text{ m}^2/\text{s}$) but is optically opaque. Due to the layer by layer nature of 3D printing, test section strength can become an issue in rotating tests. A typical testing time of 25-40 s is required, and hence, test section walls should be at least 6.35mm thick. Figure 14 shows two ways to record TLC color change in internal channel heat transfer study.

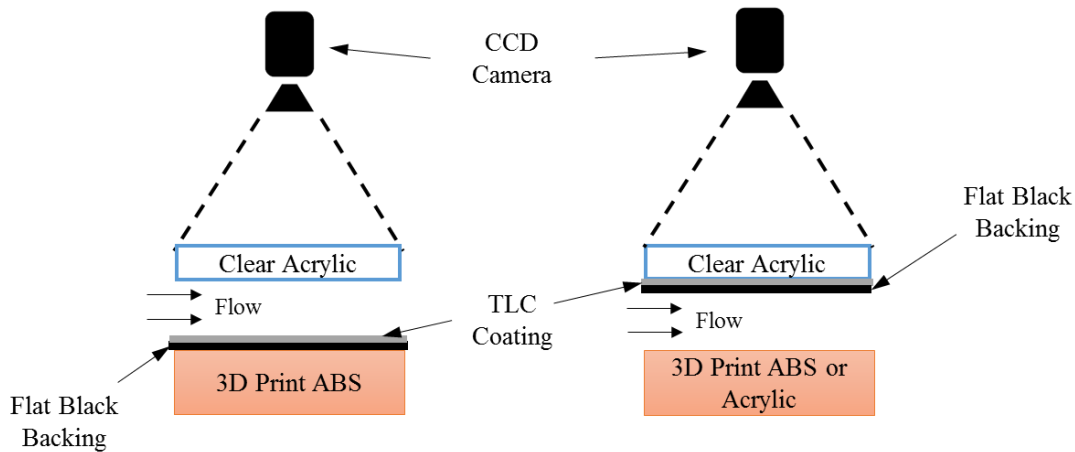


Figure 14. Two ways to record color change in TLCs using a CCD camera

The manufacturer of liquid crystals specifies that a 10 microns thick liquid crystal layer gives near true colors (RGB) and a fast response time [51]. With increasing thickness, colors appear milky especially towards the red end of the spectrum [51]. The thickness of the liquid crystal layer is not measured in this study, but a thorough application is ensured

through visual checks. On clear acrylics, a uniform liquid crystal coating will make the surface look translucent. On 3D printed ABS, about four liquid crystal layers are applied after a flat black paint coating to ensure uniform application. TLCs have a thermal conductivity between 0.2 – 0.4 W/mK [51], which further adds confidence to minimizing 2D conduction.

4.3.2. Lighting Setup

It is desirable to illuminate the TLC coated surface evenly such that each pixel has a uniform background intensity range. As described by Ekkad et al. [50], the optimum background intensity should be under 100 (on an 8 bit scale, 0 – 255). This threshold has become lower with improvements in camera technology to capture clear videos at low lighting conditions. Nonetheless, uniform lighting of the test plate is necessary. For stationary heat transfer tests, a system of fluorescent lights and LED lights angled at 45° towards the test section is used, as shown in Figure 15. This system is mounted on a steel strut frame over the test section. The CCD camera for video recording is also placed on the steel frame.

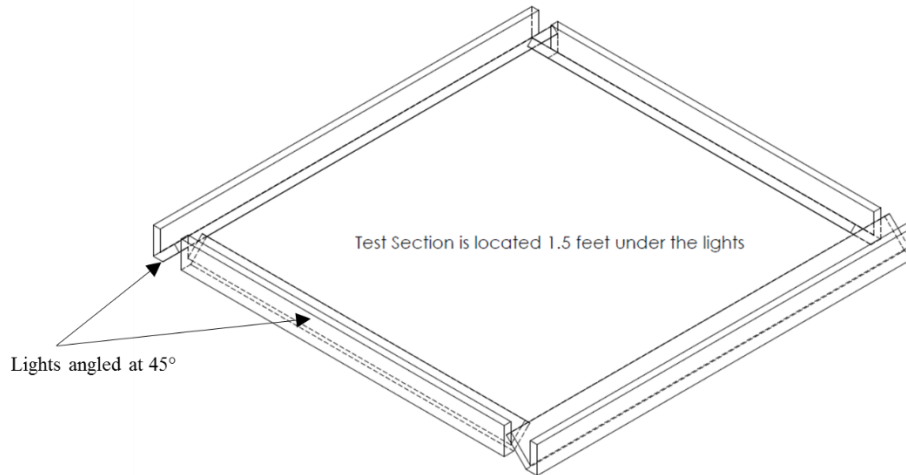


Figure 15. Lighting setup for the stationary heat transfer tests

4.3.3. Choosing a TLC Band

As noted in section 4.1, TLCs can be manufactured in various configurations. However, correct choice of TLCs can have a big impact on the accuracy of the results. Generally, it has been found that a large bandwidth TLC may have larger uncertainties in color vs. temperature relationship. A 1°C TLC band is ideal for uncertainty considerations, but gives only a few frames of color data. For example, if recording at 30 fps, total color information from TLCs will be within those 30 frames and data may be lost. A higher fps camera can rectify this problem, but would also raise the camera cost. Thus a compromise at a 5°C TLC band can be made. Also, the melting temperature of acrylic and ABS is close to 90°C , thus mainstream temperature must not exceed this limit. Below 0°C , the response time of TLC becomes higher as the molecules do not have enough kinetic energy to fold and unfold easily [51]. Through experimental trial and error, it has been found that a step change in mainstream temperature of about 20°C from the end of TLC bandwidth works best in keeping the testing time under the maximum permissible time for holding the semi –

infinite assumption. It is also important to understand the test rig capabilities of providing high or low temperatures without damaging the rig components. With all these considerations, appropriate TLC color play range can be decided upon.

4.4. Data Reduction Technique

There are two sets of data that are collected during a transient liquid crystal experiment: video recording of TLC color change and temperature measurements of the mainstream air and TLC coated surface. From these measurements, heat transfer coefficient is determined at each pixel location.

4.4.1. Calibration of TLC

The first step in data reduction is to calibrate the liquid crystal to obtain information regarding color vs. surface temperature. There are two choices in measuring TLC surface temperature. One method is to place a thermocouple on the test surface and measure surface temperature during each test run. TLCs can degrade over time as they go through cycle of temperature rise and decrease. Their response time can increase, as well as, the entire TLC band can shift to higher temperatures than the one specified by the manufacturer. By measuring the surface temperature variation at each test run, researchers can eliminate the uncertainty in TLC color change and temperature band. However, this method is susceptible to the measurement of the mainstream air temperature, rather than the surface itself. To avoid this, the second method of calibration is to run a separate test where the test surface is heated in such a way that the thermocouple does not get exposed to the hot air (or cold air). Figure 16 shows a test setup that can achieve this. A surface thermocouple

is placed on the TLC coating on an ABS plate with flat black backing and a heat gun is used to heat the test plate from the opposite side. This also eliminates the uncertainty if the thermocouple is actually measuring the TLC temperature or ABS surface temperature. The disadvantage, however, of this method is that degradation in liquid crystal with each experiment cannot be determined. Therefore, each test plate with a TLC coating should not be used for more than 10 experiments. If a new TLC coating is applied, then a new calibration should be conducted.

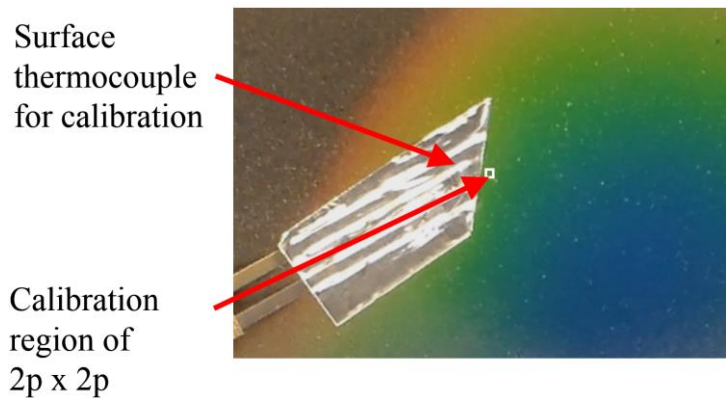


Figure 16. Calibration setup indicating surface thermocouple and calibration region

Data reduction techniques usually track a particular color's appearance during a test run and appoint the calibrated temperature to it. Green color has the highest intensity amongst all other colors. If all three colors, red, green and blue, are plotted with temperature, the green has the highest peak in the TLC bandwidth. For these reasons, peak green color was tracked and the associated calibration temperature was assigned. Figure 17 shows the peak green color for the calibration region shown in Figure 16.

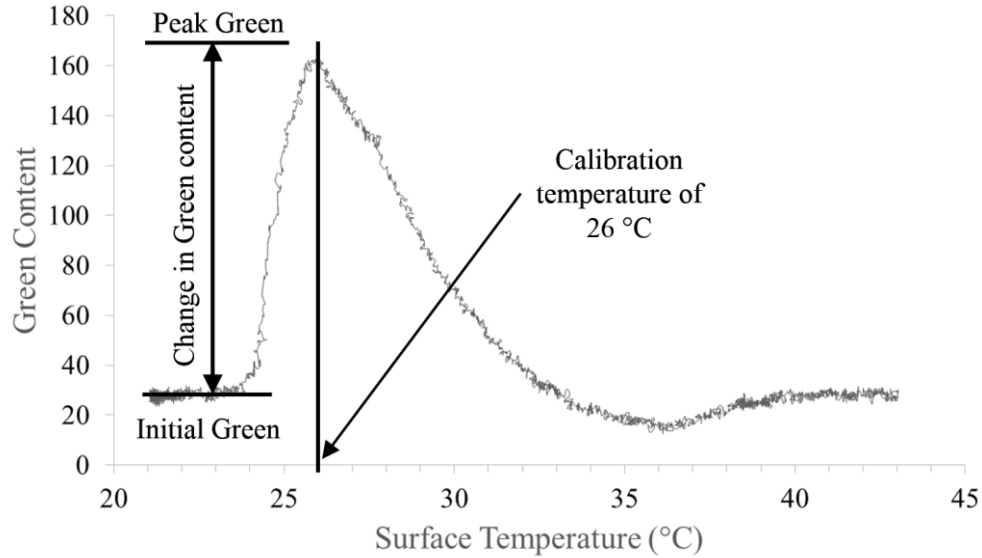


Figure 17. Results of the calibration test run for green color to surface temperature

4.4.2. Green-start Technique

The data reduction code is programmed into MATLAB. The code first reads the video file and converts each pixel into RGB values at each frame. Video cropping features in the code also allows removal of unwanted areas of video recording which reduces the data processing time. Based on the calibration thermocouple information, each pixel's green content history is tracked. Depending on the surface illumination, each pixel may not show the same peak green color as the calibration region. Thus a fixed value of green color content cannot be used for comparison of one pixel to the calibration pixel. The code uses an arbitrary threshold of change in green content. When the green color content crosses the threshold, it is said that the pixel has achieved green color.

To determine heat transfer coefficient from Equation (10) at each pixel, a time matrix is created which consists of the time taken by each pixel to cross the threshold value of green color. Material properties of the solid and air are calculated at average temperatures.

Initial temperature of the solid is measured before each test. Equation (10) is then modified in the following manner,

$$T_{(0,t),est} = T_i + \left[(T_\infty - T_i) \times \left(1 - \exp\left(\frac{h^2 \alpha_s t}{k_s^2}\right) \operatorname{erfc}\left(\frac{h\sqrt{\alpha_s t}}{k_s}\right) \right) \right] \quad (12)$$

Where $T_{(0,t),est}$ is the estimated wall temperature. Since h is not known, a value is guessed and error is calculated by,

$$Err = (T_{wc} - T_{(0,t),est})^2 \quad (13)$$

Where Err is the error and T_{wc} is the wall calibration temperature. A golden bisection method is used to minimize the error. Once the interval of the golden bisection triplet is less than one, the minimization loop exits and the final value of heat transfer coefficient is stored for that particular pixel.

4.5. Uncertainty Analysis

It is evident from Equation (12), that an explicit solution for the heat transfer coefficient is not possible. Thus, the root-sum-square method prescribed by Kline and McClintock [53] cannot be directly used. Therefore, a sequential perturbation technique, as described by Moffat [54], was used. The first step was to transform Equation (12) into a non-dimensional form. The following parameters were used

$$t = t^* \tau$$

$$\tau = \frac{D_h^2}{\alpha_s}$$

$$Nu = \frac{h D_h}{k_f}$$

$$T_{(0,t),est} = T_{(0,t),est}^* T_i$$

$$T_\infty = T_\infty^* T_i$$

The resulting equation after non-dimensionalization is

$$T_{(0,t),est}^* = 1 + \left[(T_\infty^* - 1) \times \left(1 - \exp\left(Nu^2 \left(\frac{k_f}{k_s} \right)^2 t^* \right) \operatorname{erfc}\left(Nu \left(\frac{k_f}{k_s} \right) t^* \right) \right) \right] \quad (14)$$

For uncertainty, each parameter was varied by its measurement uncertainty and its effect on Nu number was determined. Temperature measurements were varied to the extremes by the thermocouple specific uncertainty. Since it is not known how material properties of the test plate varied with temperature, they were kept constant. The time taken to reach the desired green color had an uncertainty due to the frame rate of the camera. Thus, a zero order uncertainty was assigned to time measurements (half of the frame rate). In addition to these, the error determining equation compared the estimated temperature value to the calibrated wall temperature value. Uncertainty in the temperature measurement of the calibration temperature was also accounted for. Finally, the golden bisection method's tolerance was set at one. Thus, zero order uncertainty of $\frac{1}{2}$ was used for that.

5. High Aspect Ratio Channel Featuring Different Dimple Configurations

This study focusses on addressing the missing information of heat transfer on side walls of dimples and effect of high aspect ratio channels in the open literature. Four dimple geometries, viz. diamond, square, triangular and cylindrical, were studied at three Reynolds numbers and are compared to a flat plate. For each case, detailed Nu contours are generated which are normalized by the area averaged Nu value from the corresponding Reynolds number case for flat plate. Data is also collected on the side walls of each dimple to capture heat transfer distributions. Detailed Nu contours are generated for the side walls as well. A brief numerical study is presented to show how vortices are generated inside the dimples and are correlated with the dimple wall heat transfer. At the end, each dimple case was evaluated by comparing their thermal – hydraulic performance factors.

5.1. Description of test-section

The test plates were 3D printed using ABS plastic. 3D printing was chosen as the preferred method to manufacture the plates because it provides high precision (0.178 mm resolution) and sharp edges to the dimples. Conventional manufacturing techniques would have resulted in rounded edges which was not desirable. ABS plastic was chosen because of its low thermal conductivity ($k = 0.18 \text{ W/mK}$) and low thermal diffusivity ($\alpha = 1.2e-7 \text{ m}^2/\text{s}$) to nullify conduction heat losses in the experiment. Visual access to the test plate surface was provided by a 6.35 mm thick transparent acrylic sheet with a low thermal conductivity and low thermal diffusivity ($\alpha = 1.09e-7 \text{ m}^2/\text{s}$, $k = 0.19 \text{ W/mK}$). To capture the surface temperature variation and hence the heat transfer, the test plate surface was first coated with a thin layer of flat black color paint and then by a thin layer of thermochromic liquid crystal (TLC). The temperature band of the TLC was 25°C to 30°C .

The TLC color change was captured by two dedicated cameras to capture the top view, and the side view of the dimple walls. The CCD camera (720p; 52x optical zoom) has the capacity to capture images at the frequency of 30 Hz. The focus and white balance of the camera was fixed to avoid any automatic adjustments made by the camera during a test run. The data generated by the camera is initially stored in an SDHC card and then transferred to the main work-station via a USB connection.

5.1.1. Mainstream Channel Dimensions

Figure 18 below illustrates the mainstream channel dimensions and shape. The corners of the channel were rounded instead of sharp corners. The aspect ratio for the channel was defined as the ratio of total width to the height of the channel and was determined to be 12.5.

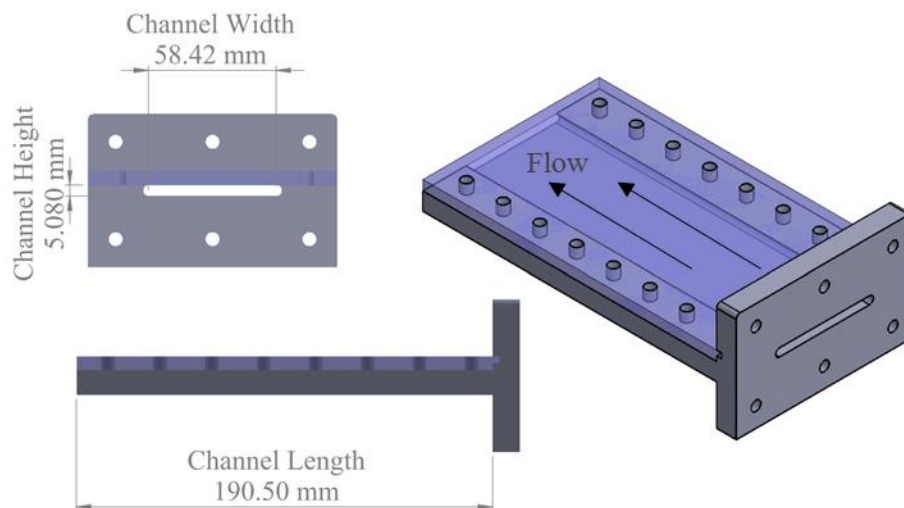


Figure 18. Mainstream channel shape and dimensions

5.1.2. Dimple Configurations

The baseline case geometry is shown in Figure 19. All the dimensions associated to Figure 19 are given in Table 1.

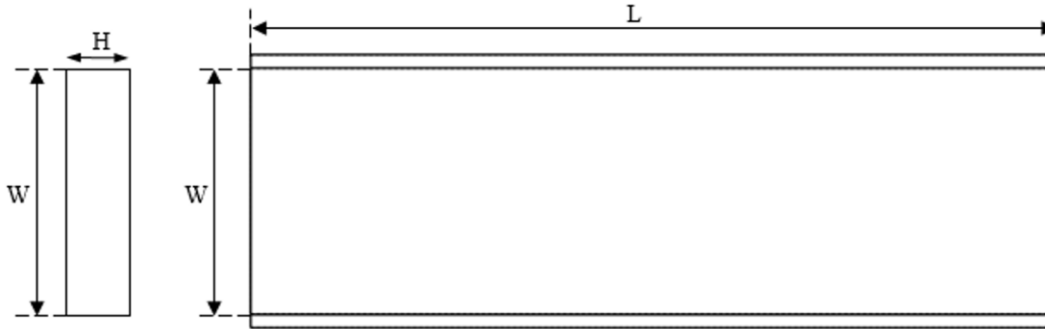


Figure 19. Baseline (un-augmented) case

Table 1. Dimensions of the flat plate shown in Figure 19

Thickness of plate, H (mm)	9.525
Length of plate, L (mm)	190.5
Width of plate, W (mm)	58.42

Figure 20 shows the four dimple configurations that have been studied. The dimensions of the dimple configurations shown in Figure 20 are given in Table 2. As shown in Figure 20, dimples are arranged in a staggered form with a consistent pitch and staggered pitch for all four configurations. The cylindrical dimple was defined as part of a cylinder rather than part of a sphere. Depth of each dimple was kept same across all the geometries as 5.08 mm. The diameter-to-depth ratio could only be defined for the cylindrical configuration, and is equal to 2.5. The other three dimples, viz. diamond, square and triangular, were designed to be within the footprint of the cylindrical dimple. By doing this, the tripping length for each dimple was kept similar.

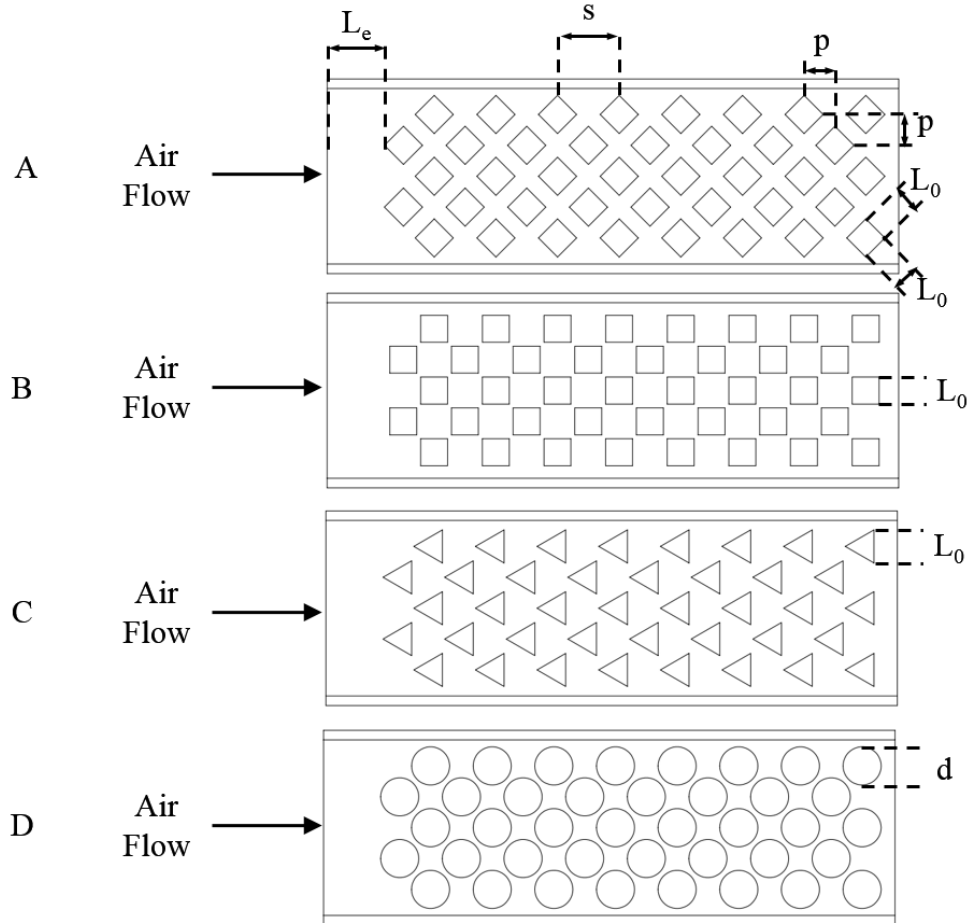


Figure 20. Dimple geometries tested, where A). Diamond, B). Square, C). Triangular and D). Cylindrical

Table 2. Dimensions of the dimple configurations shown in Figure 20

Dimple Type	L_e (mm)	d (mm)	L_0 (mm)	s (mm)	p (mm)	D (mm)	N_{total}
Diamond	19.05	-	8.980	20.55	10.27	5.080	40
Square	20.91	-	8.980	20.55	10.27	5.080	40
Triangular	19.05	-	11.00	20.55	10.27	5.080	40
Cylindrical	19.05	12.70	-	20.55	10.27	5.080	40

Figure 21 shows an isometric view of the cross-section of each dimple case. It is to be noted that each dimple has a flat end rather than having a ramp.

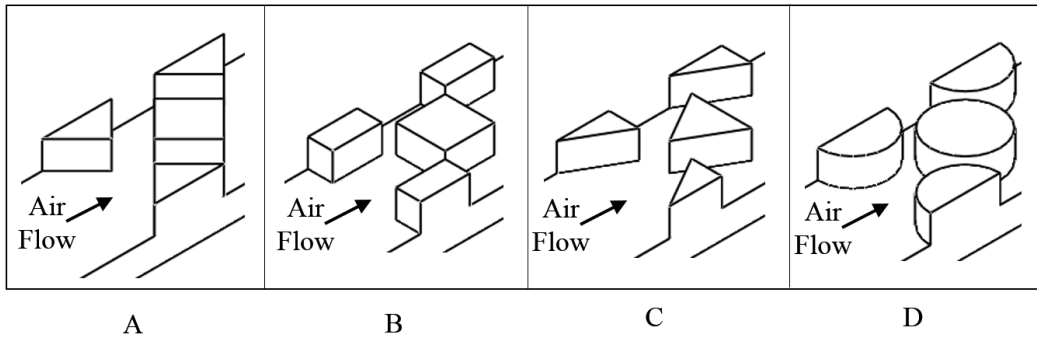


Figure 21. Cross section of the dimples: A). Diamond, B). Square, C). Triangular and D). Cylindrical

Table 3 below shows the maximum allowable testing time calculated using Equation (11) for each dimple case. For the value of thickness in the equation, the thinnest part of the dimple plate geometry was used which would be the thickness between the dimple bottom wall to the opposite side of the test plate. The testing time for each case was kept less than 30 seconds.

Table 3. t_{\max} for each case calculated using Equation (11)

Plate Type	H (mm)	t_{\max} (s)
Flat	9.525	73.8
Diamond	6.35	32.8
Square	6.35	32.8
Triangular	6.35	32.8
Cylindrical	6.35	32.8

The dimple configurations were obtained by 3-D printing, and the test-section obtained was polished using a very fine sand paper to remove any surface roughness which might contribute towards bad resolution data and unexpectedly higher heat transfer regions.

5.1.3. Numerical Simulations

To understand the flow features inside the dimples, a brief numerical simulation was conducted using Ansys CFX. In order to minimize computation time and reduce the

number of elements, only the middle strip of each dimple geometry was used, as shown in the fluid domain in Figure 22 below.

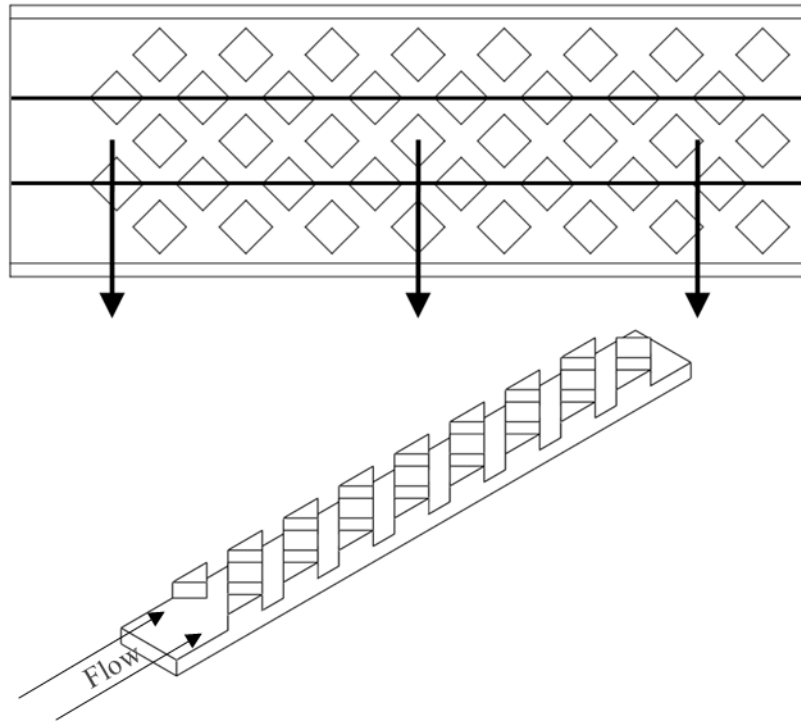


Figure 22. Dimple plate region chosen for numerical simulations

A periodic boundary condition was used on the side wall of the CFD geometry. A constant temperature of 21°C boundary condition was used on the dimple walls and mainstream channel walls as this represents the room conditions in which experiments were performed. The inlet was specified as a velocity condition with 5% turbulence intensity and a temperature of 100°C. The outlet was set at zero static pressure condition. Figure 23 below shows the unstructured mesh which was used for the analysis. A total of 19 inflation layers were used to capture the near wall effects within the dimples and the

mainstream channel. About 1.2 million elements were used for the analysis for each dimple geometry.

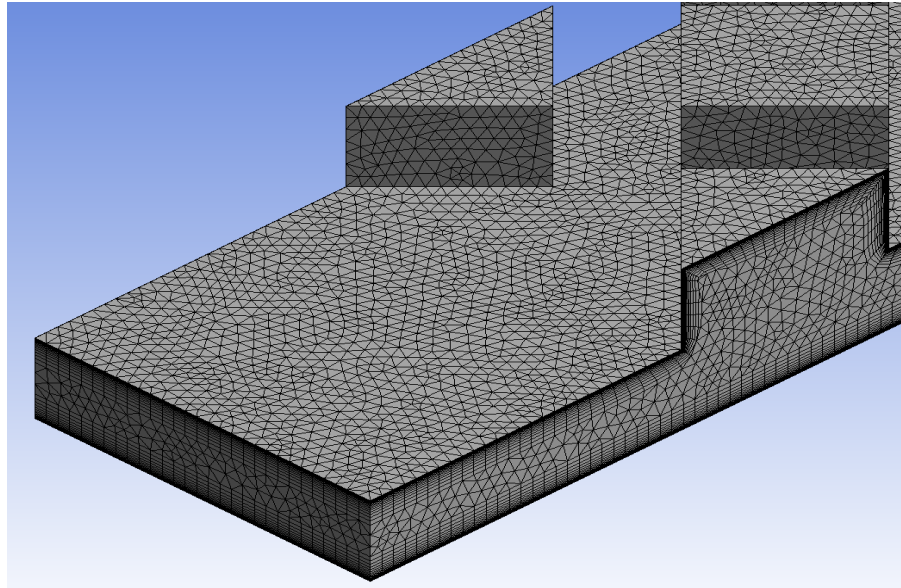


Figure 23. Meshing of the CFD region

5.2. Results and Discussion

Experiments were carried out at three Reynolds numbers, viz. 10,000, 15,000, 21,000 for the baseline case and each of the four dimple configurations. The Reynolds number is calculated using the hydraulic diameter of the inlet of the test section. The streamwise plots of Nu number for the dimple configurations are non-dimensionalized by the Nu number obtained for the baseline case. All Nu numbers are calculated using the hydraulic diameter of the inlet of the test section (consistent with Reynolds numbers). For all the figures shown beyond this point, the direction of the air flow is from left to right.

5.2.1. Baseline (un-augmented) Case – Flat Plate

The detailed Nu number contour for the flat plate at $Re = 21,000$ has been shown in Figure 24. Note that the dark spot near the entrance region is due to the presence of the thermocouple which measures the mainstream air temperature. The presence of this dark spot can be also be seen in other contours presented later. As compared to the other regions, the Nu number is significantly higher at the test-section inlet because the air is entering the test section with no boundary layer and with significantly high turbulence. Also, majority of the mass of air is centered rather than evenly spread out. This is because the converging section before the inlet changes its shape rapidly and thus the air has little length to develop and occupy the entire shape of the channel. As the flow progresses in the test section, the central jet of air diffuses and the heat transfer distribution becomes more uniform. Near the side walls, boundary layer growth occurs which lowers the heat transfer in its nearby region.

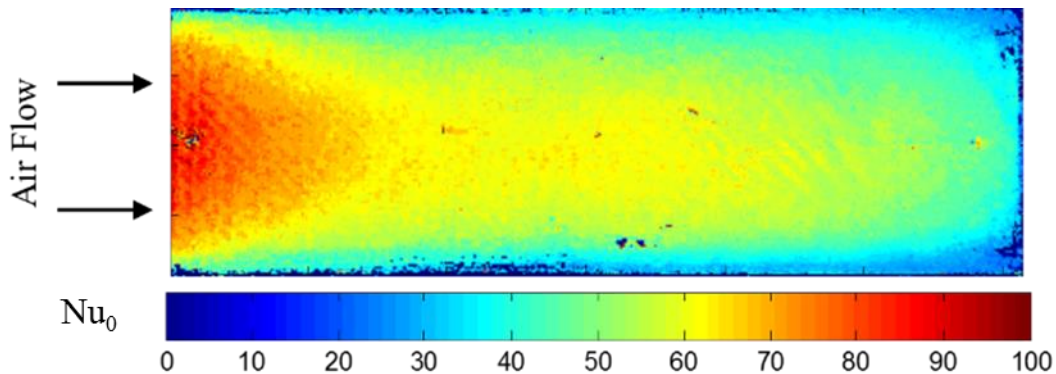


Figure 24. Nusselt number distribution for $Re = 21,000$ case for the flat plate

The spanwise averaged, stream-wise variation of Nu number for the 10,000, 15,000 and 21,000 Reynolds number is shown in Figure 25. It can be observed that, except for the $Re = 10,000$ case, the gradient of Nu number with the non-dimensional streamwise distance

has a persistent negative slope, which is indicative of developing flow due to insufficient channel length. An increase in Nu number is observed for Re = 10,000 case at the middle of the test plate but the overall trend is similar to other two Reynolds numbers.

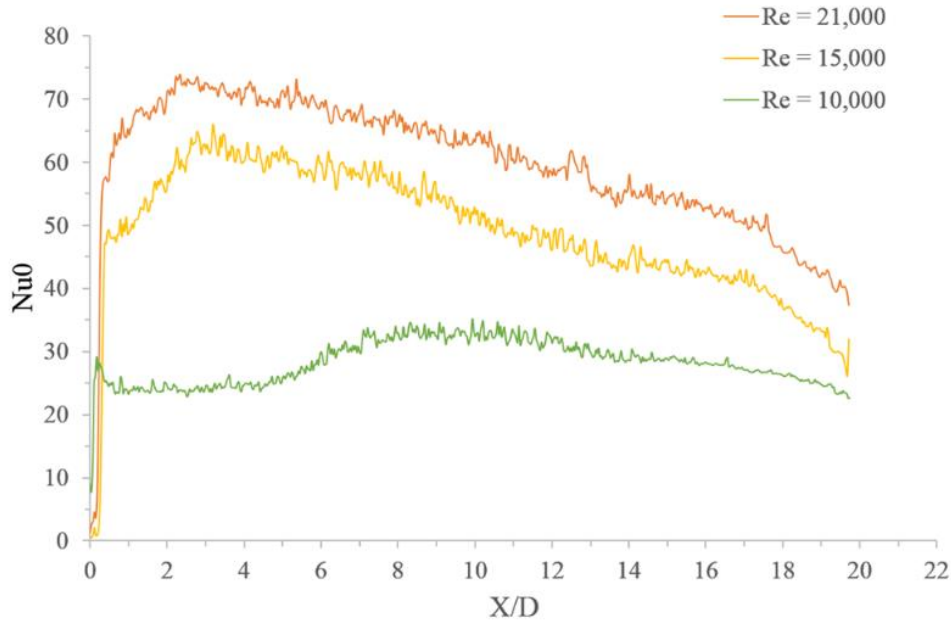


Figure 25. Spanwise averaged streamwise variation of Nu number for the baseline case for all three Reynolds numbers

Table 4 shows the comparison of area averaged Nu number values with Dittus – Boelter correlation for internal flows. The area averaged values are within $\pm 15\%$ of the predicted values even though Dittus – Boelter correlation should be applied for channels with aspect ratio ≤ 10 . In the current study, the channel aspect ratio was 12.5, nevertheless a good match between experimental values and Dittus – Boelter was observed.

Table 4. Comparison of area-averaged Nu number values for flat plate with Dittus – Boelter correlation value

Re	Flat Plate, Nu₀	Nu_{DB}
10,000	28.48	32.47
15,000	51.73	44.92
21,000	61.10	58.79

Below is case by case analysis of the dimple augmented heat transfer results. As discussed before, only the middle strip of each plate was chosen to be analyzed.

5.2.2. Diamond shaped dimples

Figure 26 shows the normalized Nu number contour for the diamond dimple case for three Reynolds numbers. These contours are normalized with respect to the area averaged Nu number obtained from the baseline geometry at the respective Reynolds number. The entrance region of each case has a Nu/Nu₀ ratio close to 1, which means that the entrance region is similar to a flat plate scenario. It can be observed that heat transfer enhancement is maximum for the Re = 10,000 case when compared with the flat plate for the same Reynolds number. This is because at higher Reynolds numbers, the air enters the test section with significantly more turbulence to cause higher heat transfer and the presence of dimples does not add much to heat transfer augmentation. Interestingly, for Re = 21,000 case, heat transfer inside the dimples is more than the Re = 10,000 case. This change can be attributed to stronger vortex formations inside the dimples for the 21,000 case as compared to the 10,000 case.

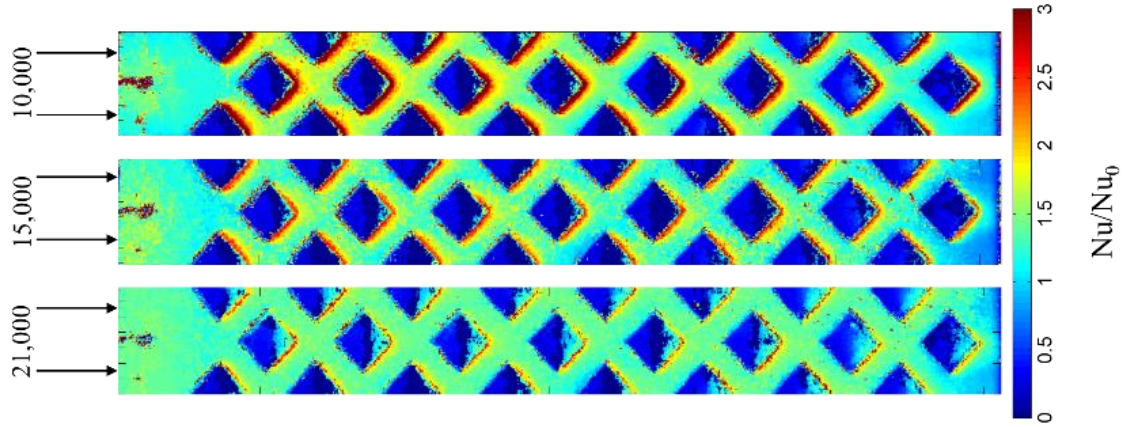


Figure 26. Detailed normalized Nu number plot for diamond dimples for all three Reynolds numbers

The streamwise variation of spanwise averaged Nu number is given in Figure 27. The values are normalized with the area averaged Nu number values from the corresponding flat plate case. The initial spike in the values is because of the presence of the thermocouple. As discussed before, the heat transfer enhancement for $Re = 10,000$ case is more than the other two cases. A good periodicity can also be seen from one row of dimples to other when moving downstream.

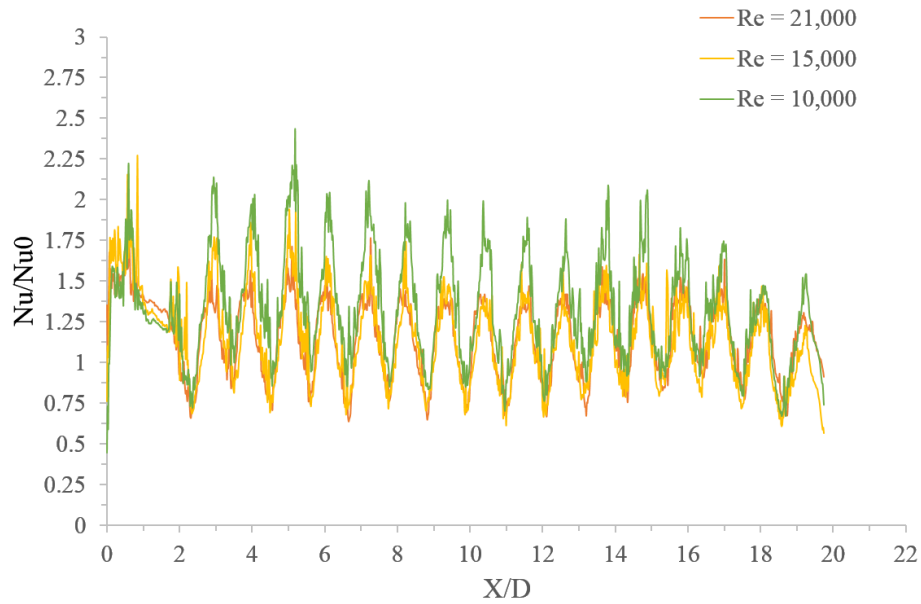


Figure 27. Spanwise averaged streamwise variation of Nu number for diamond dimple case for all three Reynolds numbers

5.2.3. Square shaped dimples

Normalized Nu number contours are shown in Figure 28 for square dimples. Similar to the diamond dimples, heat transfer enhancement is higher for the $Re = 10,000$ case than the other two cases. The square dimples, however, perform better than the diamond dimples as heat transfer enhancement travels further downstream than in the diamond dimples. This is possibly because of an overall larger tripping length offered by the square dimple than the diamond dimple. Only the centerline length of the diamond dimple has a similar tripping length to square dimple, which in comparison offers a uniformly large length over its entire geometry. Thus, boundary layer reattachment may occur sooner in diamond dimples which reduces the heat transfer enhancement in its immediate downstream region.

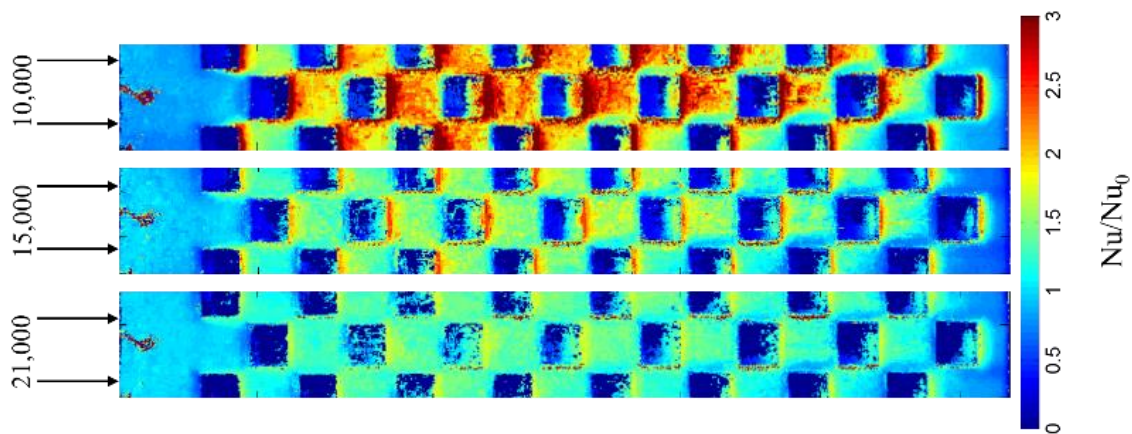


Figure 28. Detailed normalized Nu Number plot for square dimples for all three Reynolds numbers

The spanwise averaged variation of the normalized Nu number in Figure 28 shows similar trends to Figure 29 and expectedly, heat transfer peaks are higher after each square dimple row when compared to diamond dimples.

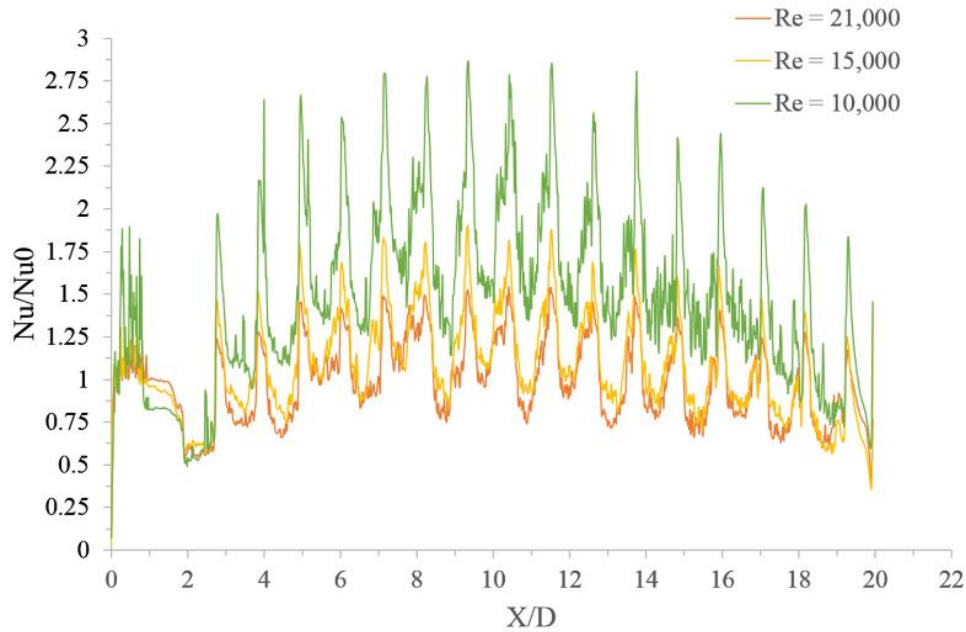


Figure 29. Spanwise averaged streamwise variation of Nu number for square dimple case for all three Reynolds numbers

5.2.4. Triangular Shaped Dimples

Similar to the above-mentioned cases, detailed Nu number contours are shown in Figure 30 for triangular dimples. The trend of higher heat transfer enhancement for Re = 10,000 case continues in triangular dimples as well. The overall heat transfer enhancement for Re = 10,000 case seems higher compared to the diamond and square dimples for the same Reynolds number, but this may be an anomaly. Figure 31 shows the spanwise averaged Nu number plot for the triangular dimples. The observed trends are similar to the previously discussed dimple cases.

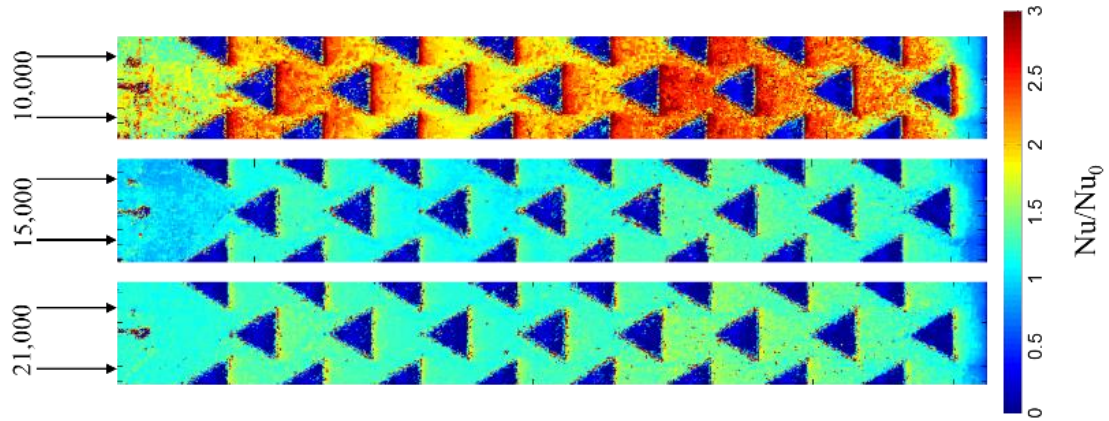


Figure 30. Detailed normalized Nu number plot for the triangular dimples for all three Reynolds numbers

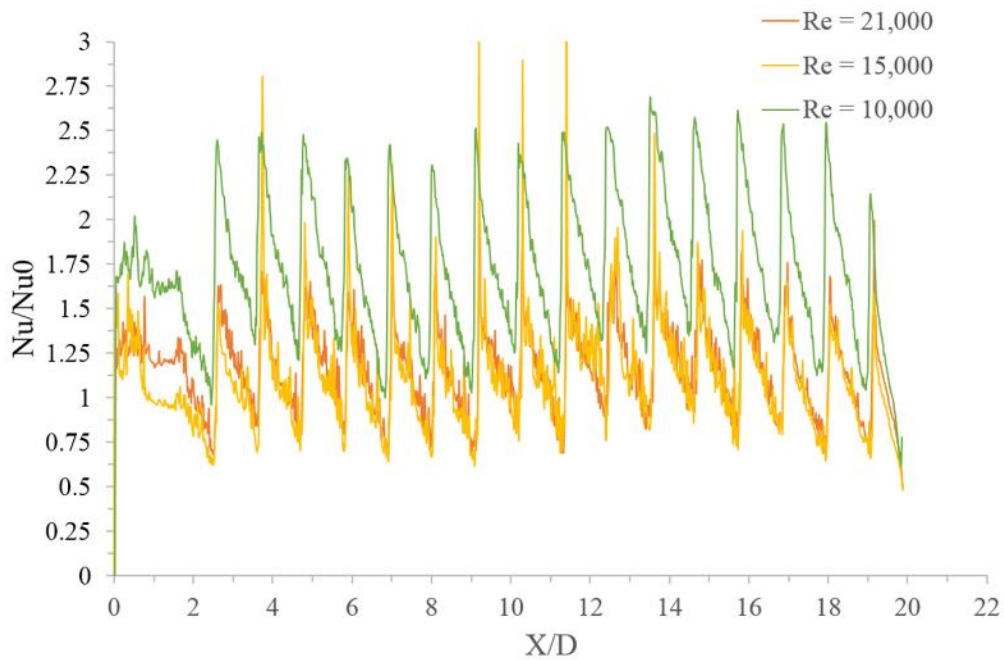


Figure 31. Spanwise averaged streamwise variation of Nu number for triangular dimple case for all three Reynolds numbers

5.2.5. Cylindrical Shaped Dimples

Detailed Nu contours for the last dimple geometry is shown in Figure 32. Compared to the other three dimples, the cylindrical dimple has the largest footprint and thus covers the maximum overall area on the test plate. Due to the bigger shape, the data resolution inside

the cylindrical dimples is better than the rest of the cases. As observed before, the heat transfer enhancement for the $Re = 10,000$ case is higher than the other two Reynolds numbers.

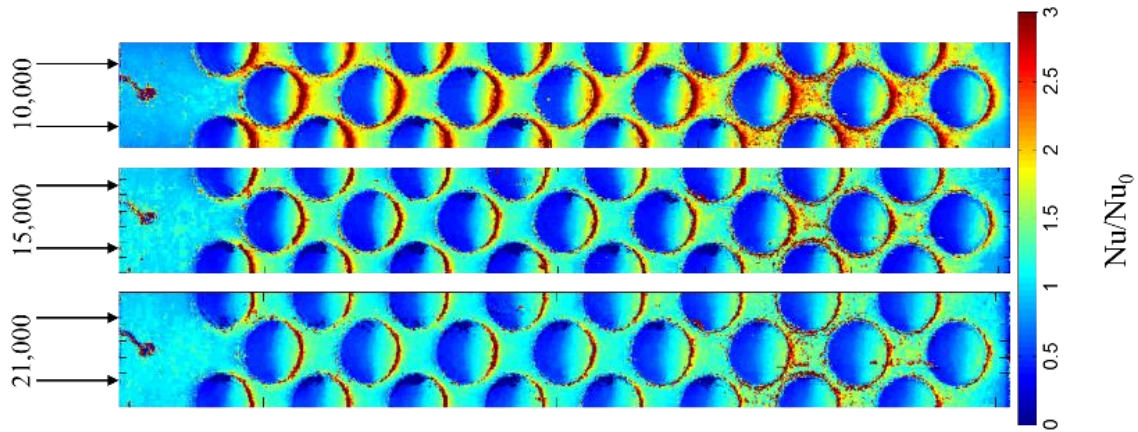


Figure 32. Detailed normalized Nu number plot for cylindrical dimples for all three Reynolds numbers

Figure 33 shows the spanwise averaged Nu number plot for cylindrical dimples. A slight increase in heat transfer is observed near $X/D = 16$ which is probably due to the interaction of different vortices produced upstream of this location.

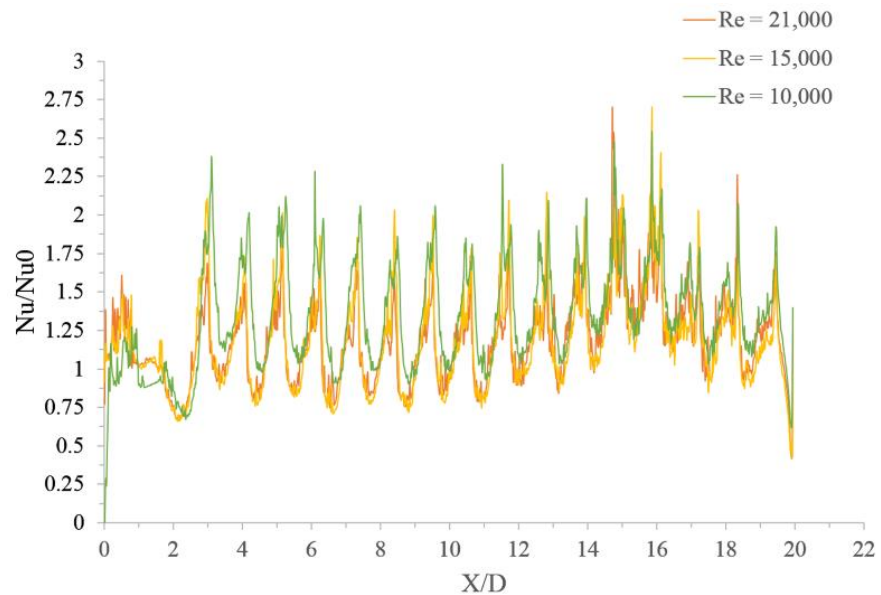


Figure 33. Spanwise averaged streamwise variation of Nu number for cylindrical dimples for all three Reynolds numbers

5.2.6. Heat Transfer on Dimple End Walls

Since the dimples cover a large area on the test plate, it is also important to understand the heat transfer distribution on the end wall of the dimples. Figure 34 shows detailed Nu number contours inside diamond dimples. Note that actual Nu number contours are presented and not the normalized Nu number contours as comparison is drawn between different dimple shapes but not with the flat plate. As expected, Figure 34 shows that with an increasing Reynolds number, higher Nu numbers are observed inside the dimples. For $Re = 10,000$ and $15,000$, the heat transfer near the leading edge of the dimples was so low that the TLC did not change color within the t_{max} obtained from Equation (11). Thus, there is a no data region present at that location. For $Re = 21,000$, TLC color change was observable and thus good resolution data was obtained.

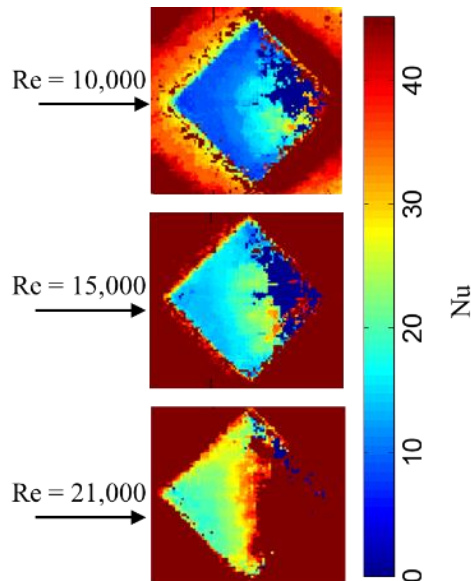


Figure 34. Detailed Nu number contours on diamond dimple end wall

The mechanism of flow into the dimples was explored using numerical analysis. Figure 35 shows a side view of the dimples with velocity vectors plotted for $Re = 10,000$ case for

diamond dimples. Air enters the dimple from the left, hits the leading edge wall and recirculates to join the mainstream. The recirculation path taken by air deposits heat into the end wall of the dimple. With increasing Reynolds number, this recirculation is stronger and thus higher heat transfer is observed.

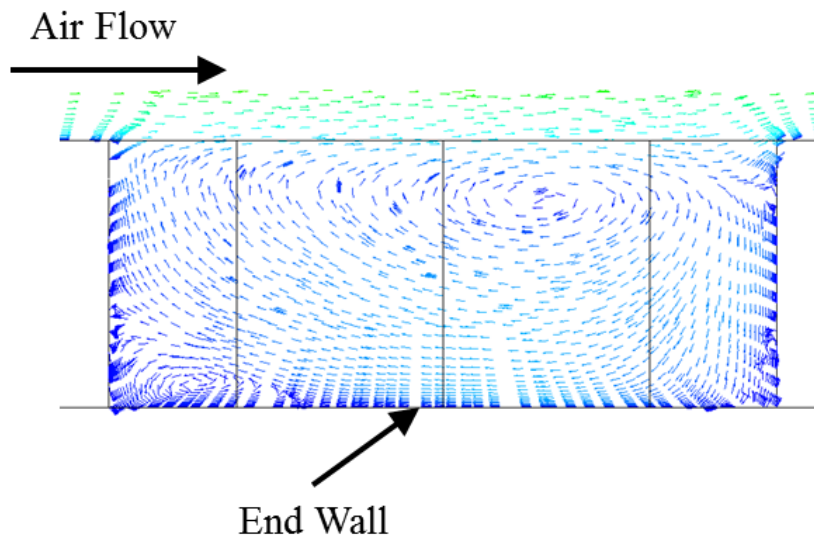


Figure 35. Air flow mechanism inside diamond dimples for $Re = 10,000$ case

Similar heat transfer trends, but with higher Nu number values, were observed for square dimple end wall. Figure 36 shows detailed Nu number contours and air flow stream lines inside a square dimple at $Re = 10,000$. The recirculation of air is much stronger in square dimples when compared with diamond dimples. This explains higher heat transfer near the leading edge of the square dimple end wall for the same Reynolds number.

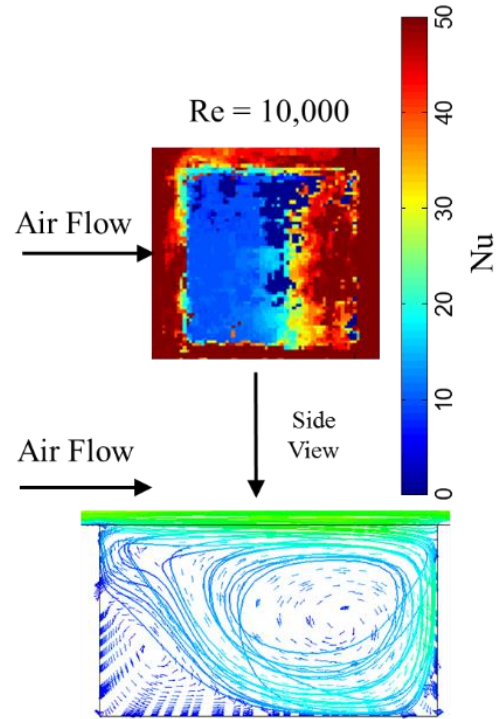


Figure 36. Detailed Nu number contours on square dimple end wall and flow streamlines showing air flow mechanism at for $Re = 10,000$ case

Figure 37 shows Nu number contour for triangular dimple end wall. This case had the lowest heat transfer amongst all the other dimple cases. Explanation for this can be observed from velocity vectors in Figure 37. There is no major air recirculation inside the triangular dimple. For $Re = 10,000$ case, heat transfer was low enough to not cause color change in TLC applied on the dimple end wall.

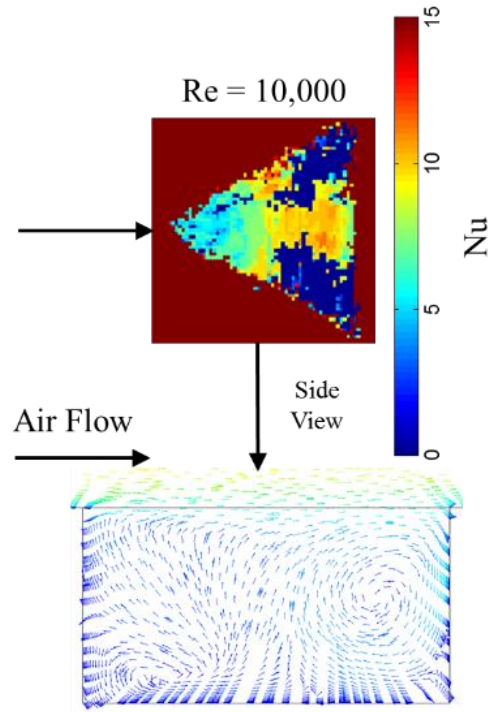


Figure 37. Detailed Nu number contours on triangular dimple end wall and flow streamlines showing air flow mechanism

Due to the large size of cylindrical dimples, high quality experimental data was observed inside the dimples. Figure 38 shows the detailed Nu number contour for cylindrical dimple end wall and velocity vectors showing air flow mechanism inside the dimple. Air recirculation pattern and strength of the vortex are similar to the square dimple case. The end wall region near the trailing edge observes an impingement type heat transfer enhancement. As this air traverses the end wall towards the leading edge, heat transfer steadily decreases until the air rises to mix with the mainstream air.

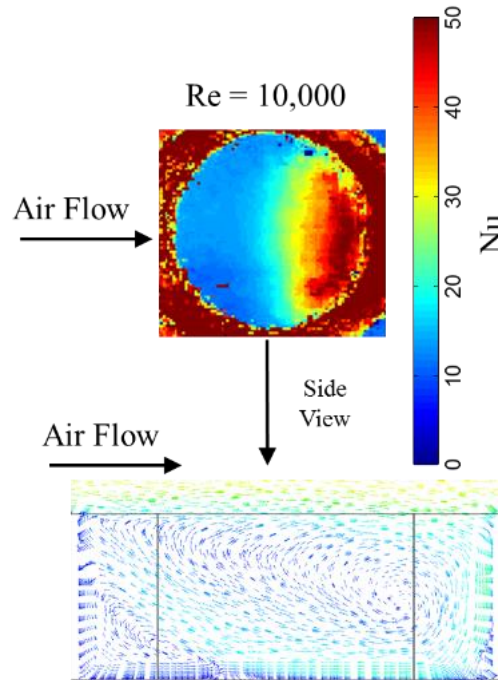


Figure 38. Detailed Nu number contours on cylindrical dimple end wall and flow streamlines showing air flow mechanism

5.2.7. Heat Transfer Behavior on the Side Walls

The heat transfer behavior inside the side wall is of particular interest in the case of dimples. The bottom surface of the dimples show a low Nu number since the mainstream air gets trapped in the cavity. The recirculation of the air inside this cavity, produces a Nu number distribution along the wall. This distribution, if captured, has the potential to illustrate the behavior of the recirculation inside the cavity. It is particularly difficult to capture this behavior as the light conditions inside the cavity are non-optimal for video recording, especially in the case of diamond and triangular dimples. Therefore, Nu number contours are shown only for the cylindrical and square dimple shapes. Figure 39 shows the Nu number distribution for the cylindrical dimple for $Re = 21,000$ case. As mainstream air enters the dimple, the recirculation of air from the trailing edge (right side) to the leading

edge (left side) is observed. The spiral showing the vortex direction validates the numerical simulation prediction given in Figure 38.

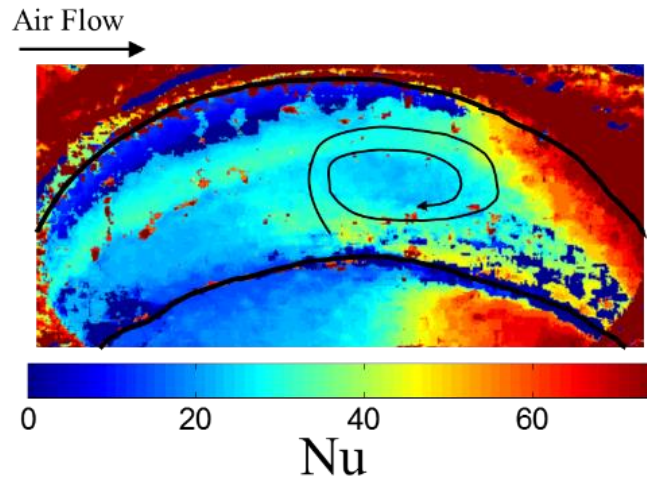


Figure 39. Nu number distribution on side wall of cylindrical dimples at $Re = 21,000$

Figure 40 shows velocity vectors which illustrate air recirculation in the vertical direction inside the dimples. Flow travels along the curved walls from the leading and trailing edges simultaneously. As it travels, heat transfer occurs on the curved walls and a low heat transfer region is observed where the two recirculating flow patterns interact.

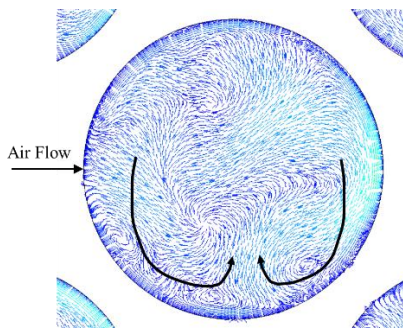


Figure 40. Air recirculation when viewed from the top

Figure 41 below illustrates side wall heat transfer in square dimples at $Re = 21,000$. For clarity, a video snapshot is also given. As predicted by CFD in Figure 36, the recirculation inside the dimple is the major reason for high heat transfer.

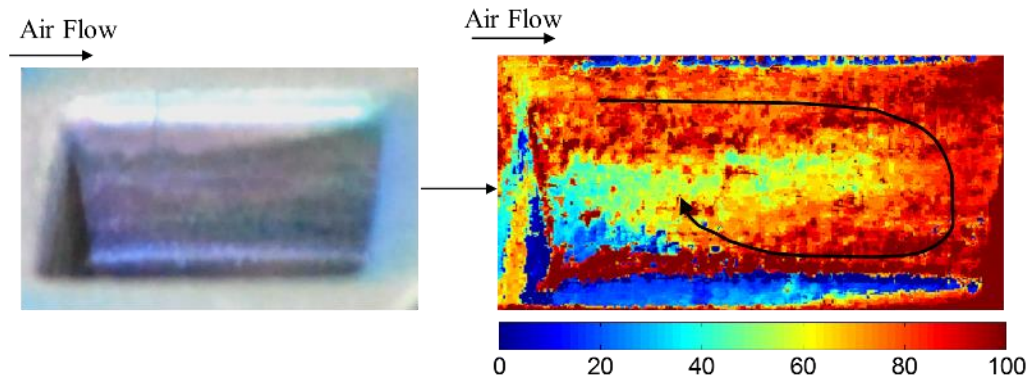


Figure 41. Nu number distribution on side wall of square dimples at $Re = 21,000$

5.2.8. Thermal – Hydraulic Performance of the Dimples

The dimples enhance heat transfer in the channel but come with a penalty of higher pressure drop when compared to the flat plate scenario. Table 5 presents the pressure drop across the channel for the five geometries that were analyzed in this study. Cylindrical dimples have the highest pressure drop penalty, whereas diamond and triangular dimples have similar pressure drop as the flat plate. The small difference in the values can be attributed to the error in the digital manometer that was used to measure the pressure drop.

Table 5. Pressure drop for all five dimple geometries analyzed in this study

Dimple Type	Pressure Drop, Δp (Pa)		
	10,000	15,000	21,000
Flat (Δp_0)	122	274	523
Diamond	113	274	523
Square	156	361	785
Triangular	110	274	523
Cylindrical	262	573	1158

To characterize if the increase in heat transfer warrants the higher pumping power requirement, a thermal – hydraulic performance factor is calculated as given by Equation (1). Table 6 shows the thermal – hydraulic performance of each dimple case. Triangular and diamond dimples perform the best amongst all the cases. Cylindrical dimples are the worst performers because of higher pressure drop penalty. Since the area covered by the cylindrical dimples is the largest, more pumping power is required to achieve the same Reynold numbers.

Table 6. Average Nu number ratio, pressure drop ratio, and thermal – hydraulic performance factor for all four dimple geometries

Dimple Type	Reynolds Number	Nu/Nu₀	($\Delta p/\Delta p_0$)^{1/3}	η
Diamond	10,000	1.37	0.97	1.40
	15,000	1.31	1.00	1.31
	21,000	1.25	1.00	1.25
Square	10,000	1.67	1.09	1.54
	15,000	1.20	1.10	1.09
	21,000	1.20	1.14	1.05
Triangular	10,000	1.84	0.97	1.91
	15,000	1.21	1.00	1.21
	21,000	1.29	1.00	1.29
Cylindrical	10,000	1.36	1.29	1.06
	15,000	1.20	1.28	0.94
	21,000	1.21	1.30	0.93

5.3. Uncertainty Analysis

Using the method described in the uncertainty section, uncertainty in Nu number for the flat plate and each dimple case was determined. Table 7 shows the uncertainty values. The mainstream temperature was measured using a t-type thermocouple which has an uncertainty of $\pm 0.5^\circ\text{C}$. Liquid crystal calibration was done using a t-type thermocouple with an uncertainty of $\pm 0.5^\circ\text{C}$. Calibration temperature and initial temperature of the solid

are the main contributors to the high uncertainty values. Since 26°C calibration temperature is very close to the initial temperature of 21°C, a small change in either causes the heat transfer values to be changed drastically.

Table 7. Uncertainty in Nu number for Re = 21,000 case

Case	Nominal Nu	Uncertainty (%)
Flat	61.1	±23.0%
Diamond	76.42	±23.2%
Triangle	76.41	±23.2%
Square	72.10	±21.0%
Cylindrical	73.75	±20.3%

The uncertainty in measurement of flow Reynolds number based on the mass flow rate calculation from the differential pressure obtained from the orifice plate was found to be ±3%.

5.4. Conclusion

Detailed heat transfer distributions for four dimple geometries at three Reynolds numbers were measured in a high aspect ratio channel using thermochromic liquid crystals. Reynolds numbers of 10,000, 15,000 and 21,000 were used in the study. The color change was measured using a camera by passing hot air over a test section kept at room temperature. After calibrating the liquid crystals, a semi – infinite model assumption was then used to relate color change with heat transfer coefficient. A flat plate was first analyzed to obtain baseline data against which heat transfer enhancement by dimples was compared. Four dimple geometries, viz. diamond, square, triangular, and cylindrical were studied. Normalized Nu number contours were generated to understand the heat transfer enhancement in the mainstream region when compared with a flat plate. Detailed heat

transfer data was also presented for the dimple end wall and side walls. Due to non-optimal lighting conditions, coupled with dimple shape, diamond and triangular dimples were omitted from the side wall data results. Numerical simulation results were used to explain the flow structure inside the dimples and how they affect heat transfer distribution.

In conclusion, heat transfer data suggested that heat transfer enhancement when compared to flat plate at $Re = 10,000$ for all dimple geometries is higher than at the other two Reynolds numbers. This is due to inherently higher turbulence for high Reynolds numbers which increases heat transfer in flat plate, while the presence of dimples does not enhance heat transfer as much. The dimple end wall heat transfer data suggested higher heat transfer in square and cylindrical dimples than diamond and triangular dimples. The reason for this is stronger air recirculation inside the dimples which promote heat transfer. The air is mostly stagnant in diamond and cylindrical dimples. Side wall heat transfer data was presented for the cylindrical and square dimples. The Nu number contours validated the flow prediction from the numerical simulations inside the dimples. To study the overall benefit of the four dimple geometries, a thermal – hydraulic performance factor was computed for each geometry. Triangular and diamond dimples performed better than the other two because of lower pressure drop penalty.

6. Rotating Two-Pass Channel with Impingement under High Reynolds Number

Most of the published work on rotating impingement focused on the jets in the leading edge region, which is a typical usage of impingement in turbine blades. Very few studies were conducted on use of impingement under rotating conditions in the radially outward channels. This study builds on the design developed by Pamula et al. [55] which employs jet holes to replace U-turns in between two serpentine cooling channels. Higher heat transfer was reported, when compared with 180-degree turn channels as reported by Wagner et al. in [41], which offsets the higher pressure drop penalty of the jet impingement design. The current study further explores the effect of rotation on this impingement design. The Reynolds number based on the channel diameter ranges from 25,000 to 100,000 and is higher when compared with previous studies. The rotation number ranges from 0 to 0.14. A transient liquid crystal method was employed in the measurement of local heat transfer coefficients. Detailed Nu number plots were generated to study the effect of rotation on local heat transfer distribution and values.

6.1. Test Section Geometry

Figure 42 shows the schematic of test section, the air flow direction and the placement of jets. All the experimental parameters are given in Table 8. The test section is a two-pass channel with a 25.4 mm square cross section and a 6.35 mm divider wall. The length of the concerned region of the channel is 6 times the channel width. Two rows of impinging jet holes were placed in the divider wall to transfer the coolant to the downstream channel. Each row contains 10 jets and the jet diameter is $1/4^{\text{th}}$ the channel width. Both streamwise

and spanwise pitches of jets are two times the jet diameter at the jet inlet. The angle between the target surface and the jet axis is 20 deg. The averaged rotation diameter for the entire test section is 15.5 times the channel diameter. Four Reynolds numbers ranging from 25,000 to 100,000 were tested under four rotation speeds, which include 0, 250, 500 and 700 rpm. As heat transfer on leading and trailing surfaces, under rotating condition, is different, a total of 28 sets of data is obtained.

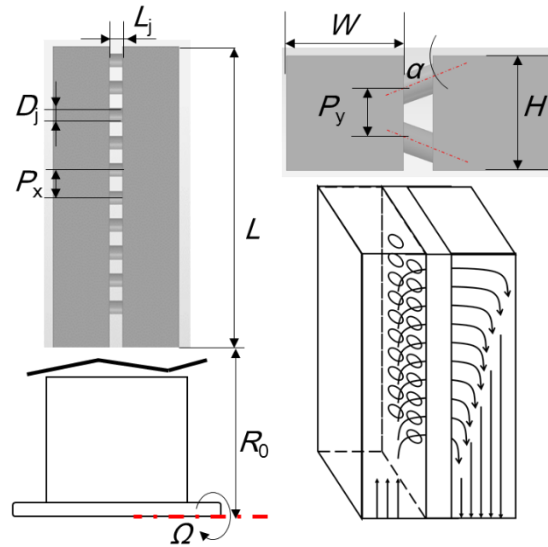


Figure 42. Definition of geometrical parameters of tested model under rotating conditions

6.2. Testing Procedures

This work was performed on the rotating heat transfer rig. The test section was mounted on the rig and balanced using counter weights. Four k-type thermocouples were used to measure temperature in the test section at the inlet, tip region, outlet and wall near the outlet. The wall thermocouple was attached to the surface using thermally conductive aluminum tape on top of the thermochromics liquid crystal coating. During each test run,

the wall thermocouple allowed wall temperature to be recorded as the liquid crystals changed color

Table 8. Dimensional and conditional parameters of the test section

Parameter	Value
D_h (mm)	25.4
H /D	1
W/D	1
L/D	6
D_j (mm)	6.35
P_x/D	2
P_y/D	2
α (deg)	20
R_0/D	15.5
n	10
Ω	0, 250, 500, 750
Re	25,000, 50,000, 75,000, 100,000

Since the transient liquid crystal technique requires a sharp change in bulk temperature, the coolant path leading to the test section was cooled using a liquid nitrogen and air mixture. During the test, when the air was allowed to flow through the chilled path, it rapidly cooled down to about 0°C (initially at 20°C) and stayed there for the entire experiment. To record the color change of the liquid crystal, a GoPro camera was mounted on the test section using a lightweight aluminum frame. The camera provided high quality videos at 1920x1080p resolution and 30 frames per second. Focus and white balance were fixed to prevent automatic adjustments which would introduce an error when relating color to temperature. A sample frame of the captured video is shown in Figure 43. The camera

frame also has the provision to hold LED lights for illuminating the test section. The LED lights are aligned at 45° angle to prevent reflections and glare onto the test section.

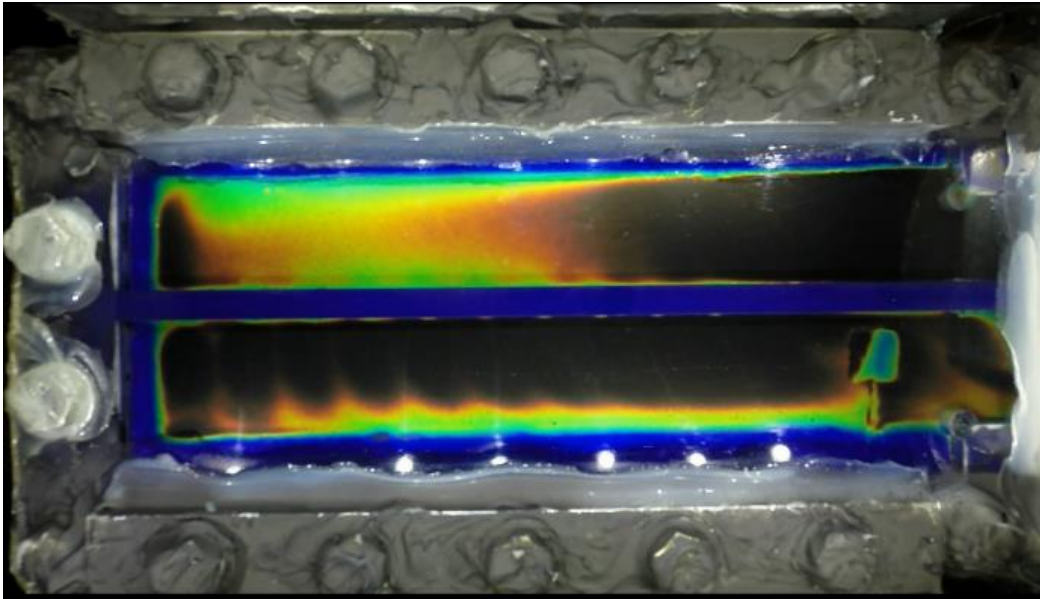


Figure 43. Color change of the target surface during liquid crystal tests

A 10° to 15° C liquid crystal temperature band was used in this study. Liquid crystal changes color between this temperature range and emits different wavelengths of visible light. Since this is an internal flow study, it is imperative that the color change is visible through the material of the test section and can be recorded by the camera. Thus, clear acrylic was the natural choice for construction of the test section. Another added benefit of using clear acrylic is that it has low thermal conductivity and prevents 2D thermal conduction during the short experiment run.

6.3. Experiment Validation

The heat transfer distribution on the target surfaces was measured both for the upstream feed channel and the impingement channel. The data was validated by the results of Pamula

et al. [55]. The geometries were similar and both measurements used the Transient Liquid Crystal technique. Results were compared for Reynolds number of 50,000. Figure 44 shows the validation of spanwise averaged Nusselt number. The measured data from this study show similar levels as seen in [55]. The local difference between the two studies is caused by different jet angles and the uncertainty of measurement.

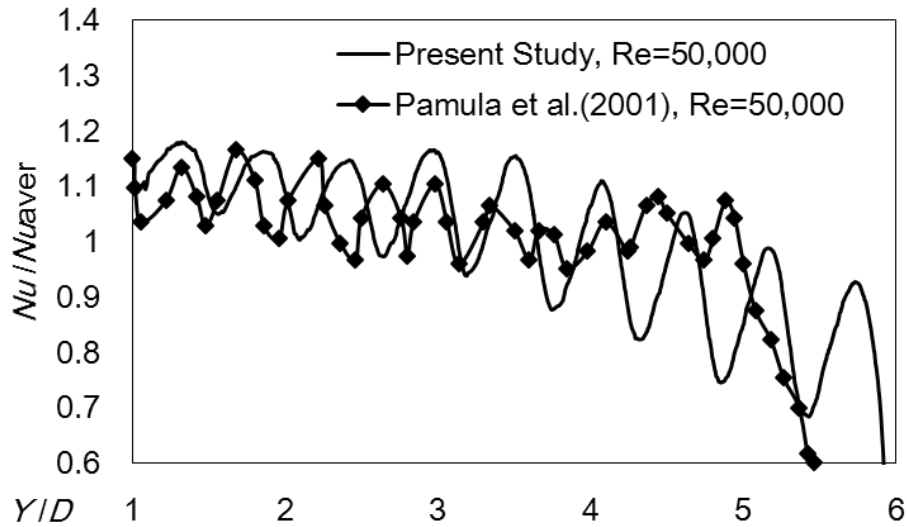


Figure 44. Comparison of Nu number between the present study and Pamula et al. [55], Pamula, G., Ekkad, S. V., and Acharya, S., 2000, “Influence of Crossflow-Induced Swirl and Impingement on Heat Transfer in a Two-Pass Channel Connected by Two Rows of Holes,” *J. Heat Transfer*, 122(2), pp. 587–597, Used under fair use, 2015

6.4. Experiment Results and Discussion

In this section, the experimental data from the TLC tests are presented, which include results under four Reynolds numbers and four Rotation numbers. Both detail distributions and spanwise/zone averaged data are displayed to show how rotation affects the heat transfer.

6.4.1. Heat Transfer Results for Stationary Tests

The top right contour plot in Figure 45 through Figure 48 shows the normalized Nu number for stationary tests. Figure 49 shows the streamwise variation of spanwise averaged normalized Nu number plots. Similar distributions of Nu/Nu_0 were observed for different Reynolds numbers. The magnitude of Nu/Nu_0 decreases with Reynolds number. The inlet channel suffers from a drop of heat transfer due to the loss of coolant mass flow rate and hence the heat transfer is reduced near the upstream closed end. In the outlet channel, impingement increases heat transfer significantly. The Nu/Nu_0 goes up to 4 near the stagnation region of impingement. The magnitude of Nu number under each jet decreases with jet number, which is associated with the mass flow distribution in jet holes, discussed previously. All Nu numbers are normalized by the Nu number Nu_0 calculated based on channel Reynolds number using the Dittus – Boelter correlation.

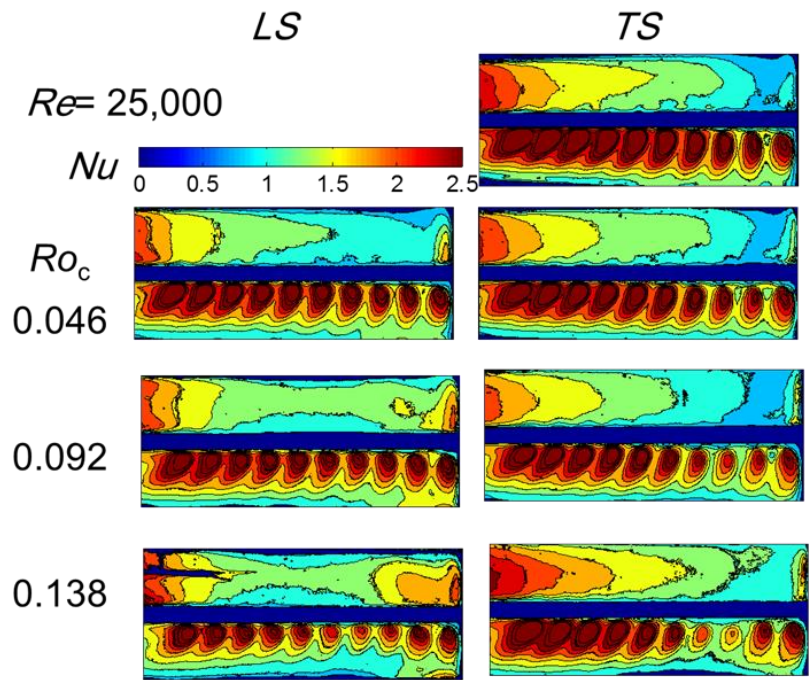


Figure 45. Detailed normalized Nu number plot for the $Re=25,000$ case at three rotation numbers

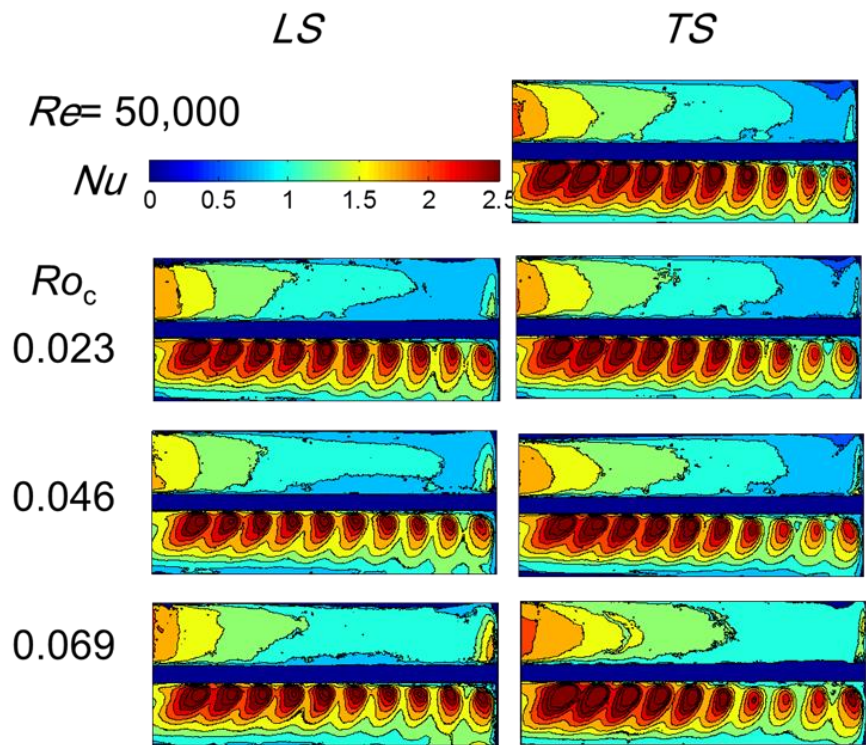


Figure 46. Normalized Nu number plot for $Re=50,000$ case

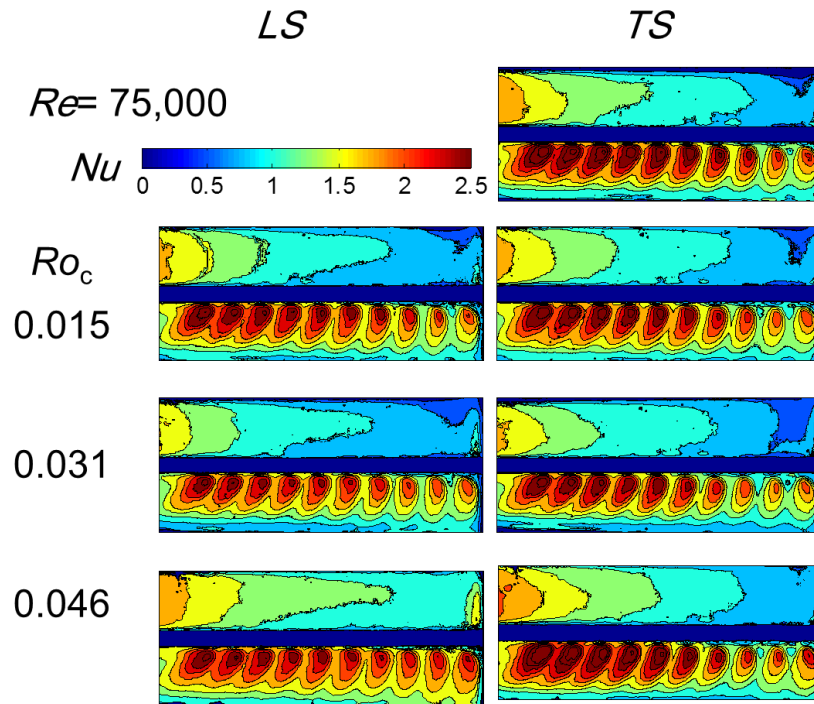


Figure 47. Nu number contours for the $Re=75,000$ case at three rotation numbers

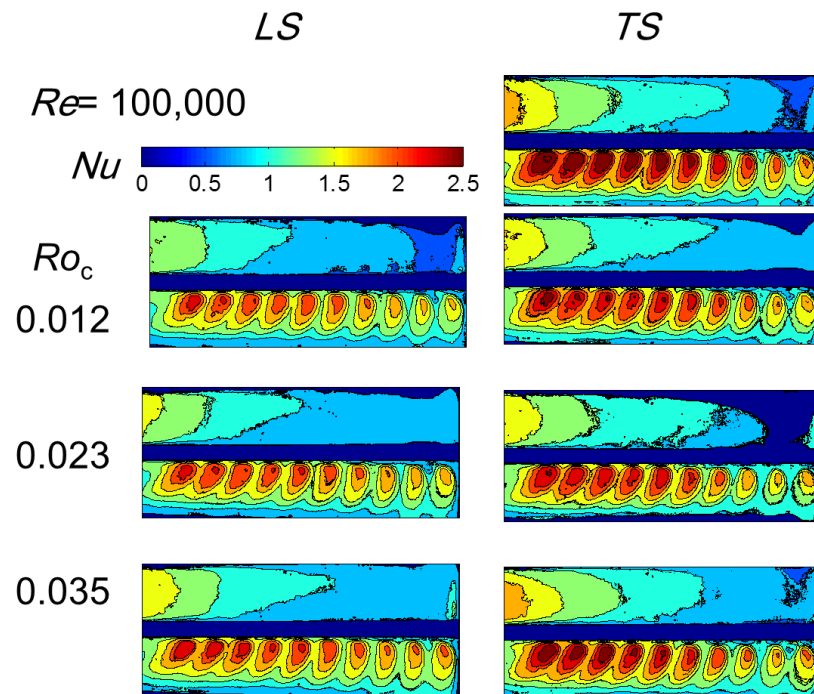


Figure 48. Nu number contours for the $Re=100,000$ case at three rotation numbers

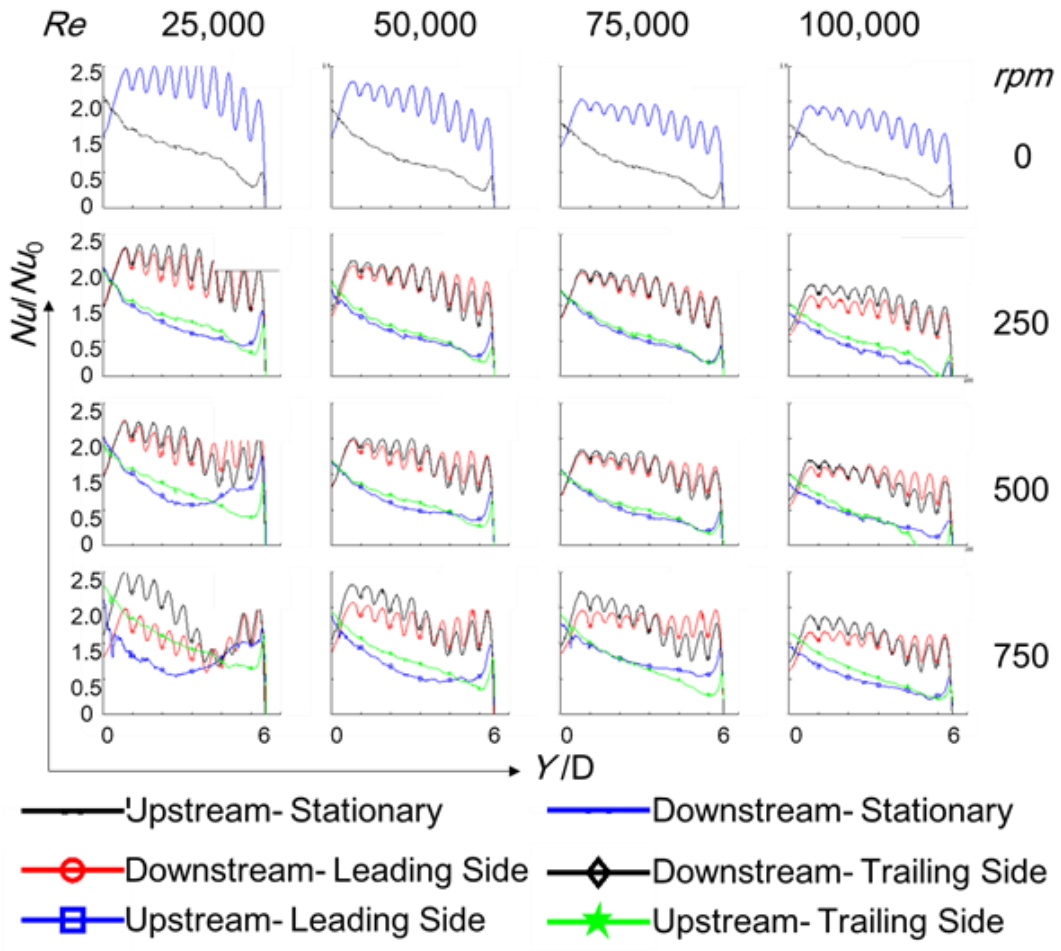


Figure 49. Streamwise variation of spanwise averaged normalized Nu number for the first pass plenum channel and second pass impingement channel under stationary and rotating conditions

6.4.2. Heat Transfer Results for Rotation Tests

Contour distributions and spanwise averaged values of Nu number ratio (rotation over stationary, Nu/Nu_s) under rotating conditions are plotted in Figure 45), through Figure 49). The Nu number ratio for rotating condition was defined differently such that the effect of rotation can be identified. Due to the direction of the Coriolis acceleration, the coolant gets pushed to the trailing side in the first pass plenum channel and the change in heat transfer is within 20%. This is a typical phenomenon for a rotating smooth channel [37]. However, the effect of buoyancy driven forces can be seen near the closed end region of the plenum channel. Since the radius of rotation at the closed end is larger, the buoyancy parameter, as defined in Equation (5), gets larger and the coolant is pushed towards the closed end. This is also referred to as a “pumping effect” and it greatly benefits the heat transfer in the plenum channel. As the rotation number increases, the Coriolis Effect and the “pumping effect” get more pronounced.

In the downstream channel with impingement, heat transfer on the leading and trailing side is reduced when compared to the stationary case. At high Reynolds numbers, the rotation number decreases, although the rotational velocity is kept constant. Thus the effect of rotation decreases at high Reynolds numbers (75,000 and 100,000 especially). The Coriolis Effect pushes the coolant to the leading side of the channel which disrupts the impinging jets. Also, the reduction of coolant on the trailing side reduces heat transfer as well. Overall, the reduction in heat transfer was up to 25% on both the sides. At high rotation numbers, the increased mass of coolant in the plenum channel’s closed end benefits the 9th and 10th jets due to the “pumping effect”, but reduces the effect of the 6th, 7th and 8th jets significantly. Another interesting phenomenon in the impingement channel

is the change in impingement footprint of the jets. At stationary and low rotation number conditions, the jet footprint is angled towards the outlet. As rotation number increases, the buoyancy forces push the coolant to the closed end. This makes the jet footprint to be orthogonal to the flow, but is detrimental to heat transfer as the coolant discharged from the jets does not leave the channel rapidly and deflects the oncoming jets.

6.5. Experimental Uncertainty and Repeatability

The first order time-constant of the liquid crystal, to characterize the time response (including the time response of the CCD cameras), is approximately 0.1 second. Experimental uncertainty magnitudes are based upon 95 percent confidence levels, and are determined using the single-sample approaches described by Kline and McClintock [53], and Moffat [54]. The uncertainty in k-type thermocouples is ± 1.0 K. The time resolution associated with the CCD cameras is approximately ± 0.1 second. As a result, the overall average experimental uncertainty for the local, time-resolved Nu number is approximately $\pm 10\%$. This uncertainty magnitude accounts for both spatial and temporal limitations of the liquid crystal in responding to the time-varying, unsteady, spatially-resolved jet flow phenomena. Regions of high and low heat transfer coefficients experience higher uncertainties either due to fast color change times or due to long color change times. Higher uncertainties in these regions could be an additional 5% higher than for most areas.

Repeatability tests were performed for all tests conditions. A sample data of the Nusselt number on the leading surface with Reynolds number of 25,000 and rotation speed 250 rpm was plotted in Figure 50. Tests under the same conditions were performed on different dates and with different temperature settings. Similar heat transfer results were obtained

with different initial temperatures, coolant temperatures and dates. The local difference between the two cases is within the uncertainty of the measurement. Thus, a good repeatability is confirmed in the present measurement setup.

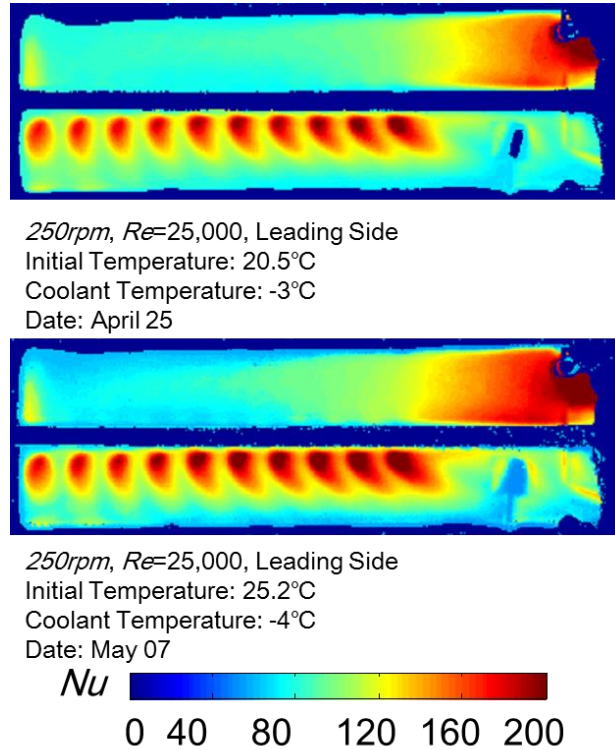


Figure 50. Repeatability of transient liquid crystal measurement in this study

6.6. Comparison with a Traditional Ribbed Cooling Channel

The design of this study, which was developed by Pamula et al. [55], was considered to replace the U-bend in cooling channels. As rotation typically causes a significant decrease of heat transfer in a ribbed channel, this study aimed to show how impingement can reduce the sensitivity of the heat transfer to rotation. To uncover this effect, a comparison between U-bend smooth channel (Wagner et al. [56]), U-bend ribbed channel (Wagner et al. [41]) and impingement channel (present study) was plotted in Figure 51. The two pass channel was divided into 6 regions according to Wagner's data. Regions 1, 2

and 3 are located upstream and regions 4, 5 and 6 are located downstream. The horizontal axis is the rotation number, which was represented as a negative value for the leading side. Wagner's rotation numbers were higher than the current study. For comparison, the trends from the present study were extrapolated to match the range of Wagner's rotation numbers. Additional testing of the proposed impingement geometry at higher rotation numbers would be beneficial.

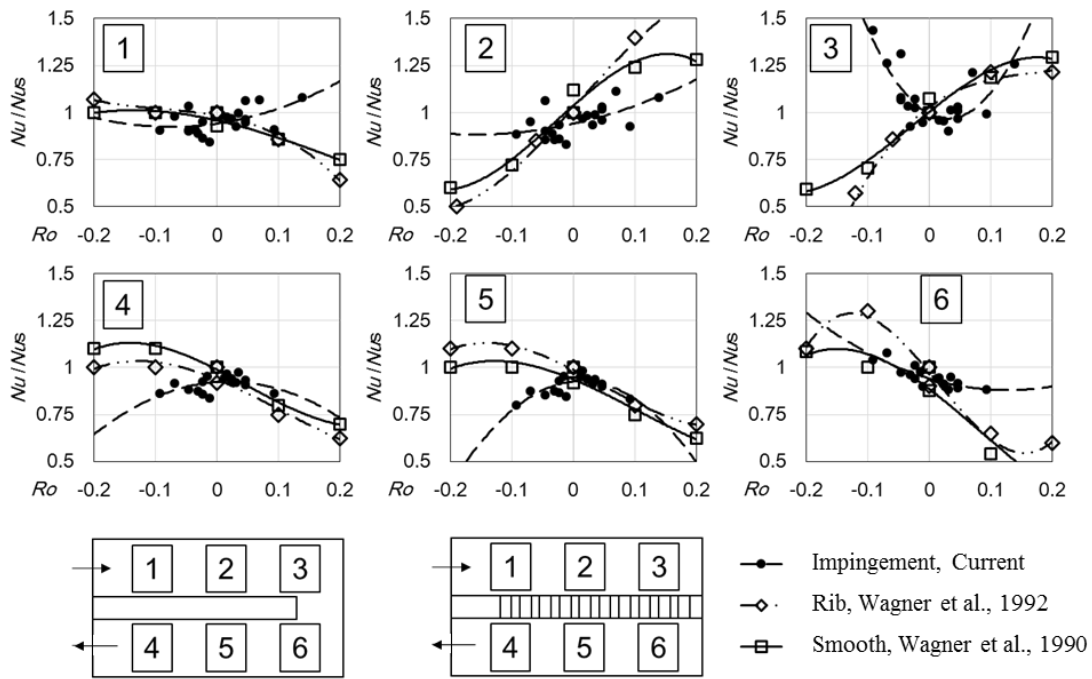


Figure 51. Comparison of the impingement study with Wagner's ribbed and smooth channel

In the upstream region, the present structure shows a lower sensitivity to rotation owing to the extraction of coolant from passage to jets. A disadvantage of impingement was observed on the leading side of the downstream channel, which is due to the asymmetric flow distribution caused by the Coriolis force. On the trailing side, impingement channel has the same Nu number ratio as the U-bend channels. Rotation significantly benefits the

leading side of upstream and trailing side of downstream near the closed end in region 3 and region 6 due to the “pumping effect”.

6.7. Conclusion

The present study considered a two pass cooling channel connected with two rows of impingement jet holes. Rotation tests were performed within a large range of parameters. The Reynolds number based on the channel diameter ranged from 25,000 to 100,000. The rotation number ranged from 0 to 0.14. A Transient Liquid Crystal (TLC) method was employed in the heat transfer measurement with and without rotation. The results indicate that:

1. Rotation reduces the heat transfer on both sides of the impingement plate, which is caused by the Coriolis force and the pressure redistribution. The local change in the present study is about 25%.
2. Rotation significantly enhances the heat transfer near the closed end because of the Centrifugal force and the ‘pumping’ effect. Within the parameters of this test, the magnitude of enhancement is 25% to 75%.
3. Compared to U-bend two pass channels, impingement channel has advantages in the upstream channel and the end region, but the performance is low on the leading side of the downstream channel.
4. In essence, this study presents a new cooling channel that may be less susceptible to rotation than a traditional ribbed channel in the mid-chord region of a rotating gas turbine blade.

7. Research Conclusion

Stationary and rotating heat transfer experiments were conducted using thermochromic liquid crystal technique. Detailed contours were generated that illustrated local heat transfer coefficient. Two heat transfer augmentation methods were studied: dimples in stationary frame and swirl induced jet impingement in rotating frame. Dimples are an attractive enhancement feature as they promote turbulent mixing without blocking the passage. Therefore, pressure drop penalties are lower. Previous studies have focused on fundamental study of flow characteristics due to dimple shapes. This study focused on experimentally measuring heat transfer on the walls of dimples of diamond, triangular, square and cylindrical shape in a high aspect ratio channel in a staggered configuration. Heat transfer was measured at three flow rate settings. Numerical simulations using Ansys CFX were used for visualizing flow inside the dimples. Firstly, channel heat transfer results were compared with literature data to make sure that the current experiments were in agreement. Then, heat transfer inside the dimples was studied in conjunction with the numerical study to identify recirculation zones in the dimple that lead to low heat transfer regions. Cylindrical dimple showed the highest heat transfer on its walls, whereas triangular dimple had the lowest. However, due to lower pressure drop penalty, triangular dimple had the highest thermal-hydraulic performance. Experimental uncertainty, using sequential perturbation technique, was less than $\pm 10\%$.

Coriolis Effect and buoyancy forces in a gas turbine blade distort heat transfer distribution. Therefore, a novel geometry was studied for heat transfer performance to replace a typical ribbed channel with a U-bend. This new geometry used two square cross section channels separated by a wall with jet impingement holes angled towards the top

and bottom walls of the outlet channel. Liquid crystal technique was used for heat transfer measurements in a rotating frame. A small, but powerful, camera was mounted with the test section to record liquid crystal color change at four flow rates and four rotation speed setting. Detailed heat transfer contours were generated. Results indicated that with increasing rotational speed, the inlet channel heat transfer is enhanced due to Coriolis Effect and centrifugal buoyancy which creates a “pumping effect” that pushes the coolant to the inlet’s end. On the other hand, outlet channel heat transfer gets reduced due to displacement of the impinging jets from Coriolis Effect. Overall, with more testing at even higher rotational speeds, the feasibility of this geometry to replace a traditional U-bend channel can be thoroughly evaluated.

Nomenclature

D	dimple diameter (mm)
d	dimple depth (mm)
D_h	hydraulic diameter channel (mm)
p	pitch of dimples (mm)
s	staggered pitch of dimples (mm)
h	local heat transfer coefficient (W/m^2K)
h_0	local heat transfer coefficient for the baseline case (W/m^2K)
H	thickness of the dimple test plate (mm)
k	thermal conductivity of ABS plastic test plate (W/mK)
k_{air}	thermal conductivity of air (W/mK)
L	length of channel (mm)
L_e	entrance length from inlet to first row of dimples
L_0	Dimple side length (mm)
Re_{D_h}	Reynolds number based on channel hydraulic diameter
t	time (s)
T_i	target surface initial temperature (K)
T_∞	mainstream flow temperature (K)
T_w	target surface wall temperature (K)
α_s	thermal diffusivity of target surface (m^2/s)
η	hydraulic performance factor
x	streamwise distance along the channel for dimple plates(mm)
Δp	net pressure drop across the channel (Pa)

Δp_0	net pressure drop across the channel for baseline case (Pa)
N_{total}	total number of dimples in a test configuration
D_j	impingement hole diameter (mm)
H	channel height of impingement channel
L	channel length
Nu	Nusselt number based on jet diameter
Nu_{aver}	Area Averaged Nusselt number
Nu_0	Nusselt number based on channel diameter in smooth channels
Nu_s	Nusselt number based on channel diameter under stationary condition
n	number of jets
P	jet hole pitch
P_x	jet hole pitch in streamwise direction
P_y	jet hole pitch in spanwise direction
Ro	Rotation number based on channel hydraulic diameter
W	channel width
X	Stream wise distance
Y	jet hole span wise pitch
Z	distance from the jet exit to the target surface
ABS	Acrylonitrile butadiene styrene (ABS)
TLC	Thermochromic Liquid Crystal
SDHC	Secure Digital High Capacity Card
CCD	Charge-Coupled Device (CCD) Camera

References

- [1] Han, J. C., and Rallabandi, A. P., 2010, "Turbine Blade Film Cooling Using PSP Technique," *Front. Heat Mass Transf.*, 1(1).
- [2] Han, J. C., Dutta, S., and Ekkad, S. V., 2012, *Gas Turbine Heat Transfer and Cooling Technology*, CRC Press.
- [3] Ligrani, P. M., Oliveira, M. M., and Blaskovich, T., 2003, "Comparison of Heat Transfer Augmentation Techniques," *AIAA J.*, 41(3), pp. 337–362.
- [4] Han, J., and Wright, L. M., 2007, "Enhanced Internal Cooling of Turbine Blades and Vanes" *The Gas Turbine Handbook*, U.S.DOE, National Energy Technology Laboratory, Morgantown, WV, pp.321."
- [5] Burgess, N. K., Oliveira, M. M., and Ligrani, P. M., 2003, "Nusselt Number Behavior on Deep Dimpled Surfaces Within a Channel," *J. Heat Transfer*, 125(1), p. 11.
- [6] Ligrani, P. M., Harrison, J. L., Mahmmod, G. I., and Hill, M. L., 2001, "Flow structure due to dimple depressions on a channel surface," *Phys. Fluids*, 13(11), pp. 3442–3451.
- [7] Mahmood, G. I., and Ligrani, P. M., 2002, "Heat transfer in a dimpled channel: Combined influences of aspect ratio, temperature ratio, Reynolds number, and flow structure," *Int. J. Heat Mass Transf.*, 45(10), pp. 2011–2020.
- [8] Won, S. Y., Zhang, Q., and Ligrani, P. M., 2005, "Comparisons of flow structure above dimpled surfaces with different dimple depths in a channel," *Phys. Fluids*, 17(4).
- [9] Slabaugh, C. D., Tran, L. V., and Kapat, J. S., 2011, "Heat Transfer in a Rectangular Channel with Dimples Applied to One Wall," *J. Propuls. Power*, 27(6), pp. 1303–1314.
- [10] Acharya, S., and Zhou, F., 2012, "Experimental and Computational Study of Heat/Mass Transfer and Flow Structure for Four Dimple Shapes in a Square Internal Passage," *J. Turbomach.*, 134(6), p. 061028.
- [11] Moon, H. K., O'Connell, T., and Glezer, B., 2000, "Channel Height Effect on Heat Transfer and Friction in a Dimpled Passage," *J. Eng. Gas Turbines Power*, 122(2), p. 307.
- [12] Shin, S., Lee, K. S., Park, S. D., and Kwak, J. S., 2009, "Measurement of the heat transfer coefficient in the dimpled channel: Effects of dimple arrangement and channel height," *J. Mech. Sci. Technol.*, 23(3), pp. 624–630.
- [13] Hwang, S. D., Kwon, H. G., and Cho, H. H., 2008, "Heat transfer with dimple/protrusion arrays in a rectangular duct with a low Reynolds number range," *Int. J. Heat Fluid Flow*, 29(4), pp. 916–926.
- [14] Lamont, J., Ramesh, S., Ekkad, S., Tolpadi, a, Kaminski, C., and Salamah, S., 2012, "Heat Transfer Enhancement in Narrow Diverging Channels," *ASME Turbo Expo*, 135(July 2013), pp. GT2012–68486.
- [15] Ekkad, S. V., and Nasir, H., 2003, "Dimple Enhanced Heat Transfer in High Aspect Ratio Channels," *J. Enhanc. Heat Transf.*, 10(4).
- [16] Ekkad, S. V., and Kontrovitz, D., 2002, "Jet impingement heat transfer on dimpled target surfaces," *Int. J. Heat Fluid Flow*, 23(1), pp. 22–28.
- [17] Han, B., and Goldstein, R. J., 2001, "Jet-Impingement Heat Transfer in Gas Turbine Systems," *Ann. N. Y. Acad. Sci.*, 934, pp. 147–161.

- [18] Viskanta, R., 1993, "Heat Transfer to Impinging Isothermal Gas and Flame Jets," *Exp. Therm. Fluid Sci.*, 6(2), pp. 111–134.
- [19] Zuckerman, N., and Lior, N., 2005, "Impingement Heat Transfer: Correlations and Numerical Modeling," *J. Heat Transfer*, 127(5), p. 544.
- [20] Ricklick, M., Kersten, S., Krishnan, V., and Kapat, J. S., 2015, "HT2008-56323 ON HEAT TRANSFER COEFFICIENT OF WETTED SURFACES IN A SINGLE INLINE," pp. 1–10.
- [21] Ricklick, M., Claretti, R., and Kapat, J. S., 2015, "GT2010-," pp. 1–10.
- [22] Ricklick, M., and Kapat, J. S., 2011, "Determination of a Local Bulk Temperature Based Heat Transfer Coefficient for the Wetted Surfaces in a Single Inline Row Impingement Channel," *J. Turbomach.*, 133(3), p. 031008.
- [23] Taslim, M. E., and Bethka, D., 2009, "Experimental and Numerical Impingement Heat Transfer in an Airfoil Leading-Edge Cooling Channel With Cross-Flow," *J. Turbomach.*, 131(1), p. 011021.
- [24] Taslim, M. E., and Khanicheh, a., 2006, "Experimental and Numerical Study of Impingement on an Airfoil Leading Edge With and Without Showerhead and Gill Film Holes," *J. Turbomach.*, 128(2), p. 310.
- [25] Taslim, M. E., Bakhtari, K., and Liu, H., 2003, "Experimental and Numerical Investigation of Impingement on a Rib-Roughened Leading-Edge Wall," *J. Turbomach.*, 125(4), p. 682.
- [26] Ibrahim, M. B., Kochuparambil, B. J., and Simon, T. W., 2005, "Cfd for Jet Impingement Heat Transfer With Single Jets and Arrays," pp. 1–15.
- [27] Parsons, J. a., Han, J. C., and Lee, C. P., 1998, "Rotation Effect on Jet Impingement Heat Transfer in Smooth Rectangular Channels With Four Heated Walls and Radially Outward Crossflow," *J. Turbomach.*, 120(1), p. 79.
- [28] Kreatsoulas, J. C., and Diego, S., 2008, "AI AA-87-2008 Experimental Data Correlations for the Effects of Rotation on Impingement Cooling of Turbine Blades AIANSAEIASMEIASSEE 23rd Joint Propulsion Conference."
- [29] Kreatsoulas, J. C., Kerrebrock, J. L., Epstein, a. H., and Rogo, C., 1985, "Effects of rotation on impingement cooling of turbine blades."
- [30] Elston, C. A., and Wright, L. M., 2015, "IMECE2012-88332," pp. 1–14.
- [31] Wright, L. M., and Elston, C. A., 2015, "Experimental Investigation of Heat Transfer in a Leading Edge, Two-Pass Serpentine Passage at High Rotation Numbers," pp. 1–13.
- [32] Hong, S. K., Lee, D. H., and Cho, H. H., 2009, "Heat/mass transfer in rotating impingement/effusion cooling with rib turbulators," *Int. J. Heat Mass Transf.*, 52(13-14), pp. 3109–3117.
- [33] Hong, S. K., Lee, D. H., and Cho, H. H., 2009, "Effect of jet direction on heat/mass transfer of rotating impingement jet," *Appl. Therm. Eng.*, 29(14-15), pp. 2914–2920.
- [34] Hong, S. K., Lee, D. H., and Cho, H. H., 2008, "Heat/mass transfer measurement on concave surface in rotating jet impingement," *J. Mech. Sci. Technol.*, 22(10), pp. 1952–1958.
- [35] Chiang, H. D., and Li, H., 2009, "Jet Impingement and Forced Convection Cooling Experimental Study in Rotating Turbine Blades," *Proceedings for the ASME Turbo Expo 2009.*

- [36] Iacovides, H., Kounadis, D., Launder, B. E., Li, J., and Xu, Z., 2005, "Experimental Study of the Flow and Thermal Development of a Row of Cooling Jets Impinging on a Rotating Concave Surface," *J. Turbomach.*, 127(1), p. 222.
- [37] Lamont, J. a., Ekkad, S. V., and Alvin, M. A., 2012, "Detailed Heat Transfer Measurements Inside Rotating Ribbed Channels Using the Transient Liquid Crystal Technique," *J. Therm. Sci. Eng. Appl.*, 4(1), p. 011002.
- [38] Lamont, J. a., Ekkad, S. V., and Alvin, M. A., 2012, "Effects of Rotation on Heat Transfer for a Single Row Jet Impingement Array With Crossflow," *J. Heat Transfer*, 134(8), p. 082202.
- [39] Lamont, J. a., Ekkad, S. V., and Anne Alvin, M., 2013, "Effect of Rotation on Detailed Heat Transfer Distribution for Various Rib Geometries in Developing Channel Flow," *J. Heat Transfer*, 136(1), p. 011901.
- [40] Han, J. C., 1984, "Heat Transfer and Friction in Channels With Two Opposite Rib-Roughened Walls," *J. Heat Transfer*, 106(4), p. 774.
- [41] Johnson, B. V., Wagner, J. H., Steuber, G. D., and Yeh, F. C., 1992, "Heat transfer in rotating serpentine passages with trips normal to the flow," 114(October 1992).
- [42] Taslim, M. E., Rahman, a., and Spring, S. D., 1991, "An Experimental Investigation of Heat Transfer Coefficients in a Spanwise Rotating Channel With Two Opposite Rib-Roughened Walls," *J. Turbomach.*, 113(1), p. 75.
- [43] Parsons, J. a., Je-Chin, H., and Yuming, Z., 1994, "Wall heating effect on local heat transfer in a rotating two-pass square channel with 90° rib turbulators," *Int. J. Heat Mass Transf.*, 37(9), pp. 1411–1420.
- [44] Johnson, B. V., Wagner, J. H., Steuber, G. D., and Yeh, F. C., 1993, "Heat transfer in rotating serpentine passages with selected model orientation for smooth or skewed trip walls," 116(October 1994).
- [45] Jang, Y.-J., Chen, H.-C., and Han, J.-C., 2001, "Flow and Heat Transfer in a Rotating Square Channel With 45 deg Angled Ribs by Reynolds Stress Turbulence Model," *J. Turbomach.*, 123(1), p. 124.
- [46] Stephens, M. A., Chyu, M. K., and Shih, T. I. P., "Computation of compressible flow and heat transfer in a rotating duct with inclined ribs and a 180-deg bend," *ASME 96-GT-192*.
- [47] Acharya, S., Dutta, S., Myrum, T. a., and Baker, R. S., 1993, "Periodically developed flow and heat transfer in a ribbed duct," *Int. J. Heat Mass Transf.*, 36(8), pp. 2069–2082.
- [48] Acharya, S., Dutta, S., Myrum, T. a., and Baker, R. S., 1994, "Turbulent Flow Past a Surface-Mounted Two-Dimensional Rib," *J. Fluids Eng.*, 116(2), p. 238.
- [49] Lamont, J. a, Roy, C. J., and Stern, C. H., 2012, "Heat Transfer in Stationary and Rotating Coolant Channels Using a Transient Liquid Crystal Technique Heat Transfer in Stationary and Rotating Coolant Channels Using a Transient Liquid Crystal Technique."
- [50] Ekkad, S. V, and Han, J.-C., 2000, "A transient liquid crystal thermography technique for gas turbine heat transfer measurements," *Meas. Sci. Technol.*, 11(7), pp. 957–968.
- [51] Hallcrest, TLC Products for Use in Research and Testing Applications.
- [52] Incropera, F. P., DeWitt, D. P., Bergman, T. L., and Lavine, A. S., 2007, *Fundamentals of Heat and Mass Transfer*, John Wiley & Sons.

- [53] Kline, S. J., and McClintock, F. A., 1953, "Describing Uncertainties in single-sample experiments," *Mech. Eng.*, 75(1), pp. 3–8.
- [54] Moffat, R. J., 1988, "Describing the uncertainties in experimental results," *Exp. Therm. Fluid Sci.*, 1(1), pp. 3–17.
- [55] Pamula, G., Ekkad, S. V., and Acharya, S., 2000, "Influence of Crossflow-Induced Swirl and Impingement on Heat Transfer in a Two-Pass Channel Connected by Two Rows of Holes," *J. Heat Transfer*, 122(2), pp. 587–597.
- [56] Wagner, J. H., Johnson, B. V., and Kopper, F. C., 1990, "Heat transfer in rotating serpentine passages with smooth walls," 113(July 1991), pp. 321–330.